

https://dspace.org/

Synchrotron studies (and applications) of diamond

Setshedi, Rhyme Kagiso

2012-02-02
http://hdl.handle.net/10539/11237

Downloaded from a DSpace repository. https://dspace.org/

Synchrotron Studies (and applications) of diamond

Rhyme Kagiso Setshedi

October 11, 2011

MSc Dissertation in Physics

submitted to

School of Physics
University of the Witwatersrand

Supervisor:

- Prof. S.H. Connell
  Department of Physics
  University of Johannesburg
  Johannesburg-South Africa

Co-Supervisor:

- Dr. Jürgen Härtwig
  Head of the Optics Group
  European Synchrotron Radiation Facility
  Grenoble-France

Declaration

I declare that this thesis is my own, unaided work. It is being submitted for the degree of Masters in Physics in the University of the Witwatersrand, Johannesburg. It has not been submitted for any other degree or examination in any other university.



October 11, 2011

(Signature of candidate)

Acknowledgments

Thanks to my lovely supervisors Prof. S. H. Connell (UJ-South Africa) and Dr. Jürgen Hätrwig (ESRF-France) and Jonathan M. Keartland (Wits-South Africa) for tirelessly helping and teaching me with big smiles on their faces. It has been a long and fruitful journey, and I will always cherish every moment we spent together. Thanks to Joh Hansen and Robbie Burns at (E6-South Africa) for their comprehensive knowledge and expertise in diamond growth, and for never thinking twice about sharing it with us. A big thanks also goes to my colleagues Denson, Lucky, Fabio and Pierre for spending sleepless nights with me at the ESRF during experiments.

The following people also afforded me time and space to explore this new adventure whilst at their employ, namely, Prof. S.H. Taole, Nkosana Mavuso and Vidius Archer. Thanks you again Marie-Anne, Barry and John for correcting my English and for always encouraging me. Special thanks also goes to my mentor, Prof. Dan Kgwadi.

And last, but not least, thanks to the "All Mighty", for giving me a lovely wife "Tsotso" and two beautiful daughters Tselane and Phemelo who always gave me courage to proceed even when times got tough. I love you all and I owe the success of this project to you. You are my true ♡ diamonds...

Abstract

This research focuses on the study of the impurities in low-strain high pressure, high temperature (HPHT) synthetic diamonds. The dominant characterisation methods are synchrotron-based x-ray techniques, supported by other conventional laboratory techniques. The research identifies the role of defects in generating long-range strain. A software programme based on the dynamical theory of x-ray diffraction has specially been developed to quantify the local changes in the lattice parameter and the local lattice inclinations (combined as the "effective misorientation" or local Bragg angle change). In recent measurements, the strain sensitivity of the (quantitative) x-ray plane-wave monochromatic topography was increased to the level of 10^{-8}. This level of sensitivity was achieved using the double crystal technique with successively higher order reflections and correspondingly, higher energy x-rays. This is a level which has never previously been accessed for diamond.

Preliminary results for this research have already contributed immensely to driving a technological development of a new range of diamond-based x-ray optical elements for modern third and fourth-generation x-ray sources like synchrotron storage rings and Free Electron Lasers (FEL), where industry (industrial diamond growers) and end-users (the synchrotrons of the world) participate collaboratively in a research and development programme.

Contents

1 Introduction **1**

1.1 Low strain diamond 1

1.2 Synchrotron-generated x-rays 3

1.3 X-ray Bragg diffraction topography 7

1.4 X-ray optical elements for third and fourth-generation synchrotron radiation sources 9

2 X-ray optical elements **12**

2.1 Diamond x-ray optics 13

2.2 High Pressure High Temperature Synthetic diamonds 14

2.2.1 Synthesis 14

2.2.2 Optical properties 22

2.2.3 Thermal properties 28

2.3 X-ray diffraction(XRD) 29

2.3.1 Response of a crystal to a plane-wave 29

2.3.2 Dynamical theory of x-ray diffraction 34

2.4 Local rocking curve measurements 39

2.5 X-ray Bragg diffraction imaging (topography) 41

2.5.1 X-ray topography techniques 42

2.5.2 Bragg and Laue geometries of x-ray topography 43

2.5.3 Basic origins of contrast in x-ray diffraction topography 45

3 Extended beam (wide area) characterization techniques 50

3.1 Integrated wave topography 52

3.2 Plane and monochromatic wave topography 54

4 Results and discussion 58

4.1 Local rocking curve broadening in type IIa HPHT diamond specimens 59

4.2 Integrated wave topography 61

4.3 Plane and monochromatic wave topography 79

5 Conclusion 101

Bibliography 104

List of appendices 112

Appendix A Analysis software 113

Appendix B Scholarly research outputs 114

List of Figures

1.1 Trends in x-ray brightness in various synchrotron sources. . . . 4
1.2 Milestones of the SCSS. 5
1.3 Visualization of defects using x-ray diffraction topography. . . 7
1.4 Possible extended defects in diamond. 8
1.5 Basic principle of x-ray monochromators. 11

2.1 A pressure-temperature phase and transformation diagram for carbon 15
2.2 A growth mechanism for High Pressure High Temperature (HPHT) synthetic diamonds. 18
2.3 Conventional diamond unit cell. 19
2.4 Growth sectors seen most frequently in the growth of near cubo-octahedral HPHT diamond crystals of type Ib. The right image is a top view of an extracted plate at the level shown by the dotted line. 20
2.5 Nitrogen and boron concentration dependencies on growth sectors observed using UV fluorescence and x-ray white beam topograph on one of the first type Ib HPHT synthetic diamond samples 21
2.6 Schematic energy level representation of the (absorption band) basic model for phosphorescence in type IIa HPHT diamond. 26

2.7 Cathodoluminiscence images, revealing a non-uniform nitrogen concentration (C_N) mainly around growth boundaries . . 27
2.8 Two x-ray rocking curves under two heat loads 0. 5 W/cm^2(left) and 1. 5 W/cm^2(right). A demonstration of excellent thermal properties of diamond suitable for x-ray optical elements for third and forth x-ray generation sources. 29
2.9 A schematic illustration of the Bragg law, $n\lambda = 2d\sin\theta$. An incident plane-wave is diffracted off successive crystal planes. . 31
2.10 Scattering of x-rays by an atom. 32
2.11 The diffraction and re-diffraction of an x-ray beam from a set of reflecting planes in Laue case. 36
2.12 Integrated intensity (reflectivity) as a function of thickness as described for non-absorbing crystals by kinematical and dynamical theories 36
2.13 An example of a reflectivity curve (known as the Darwin curve) of a thick non-absorbing silicon crystal [111] Bragg reflection. The region with R=1 is flat (top had shape) due to *interference total reflection* and the maximum of the reflectivity curve is shifted by the refraction correction $\Delta\theta_0$. The curve has been calculated using the XOP simulation software package. 37
2.14 Reflectivity curves for silicon and diamond. The full width at half maximum w_h^θ for the two curves is illustrated in both curves. The reflectivity curves were calculated using XOP software from ESRF. 40

2.15 a) Interstitial impurity atom, (b) Edge dislocation, (c) Self interstitial atom, (d) Vacancy, (e) Precipitate of impurity atoms, (f) Vacancy type dislocation loop, (g) Interstitial type dislocation loop and (h) Substitutional impurity atom. 41
2.16 Schematic "definition" of an extended beam (example for the symmetrical Laue or transmission case). 43
2.17 A scheme of the basic topographical techniques. 44
2.18 (a)Laue and (b)Bragg geometries of x-ray topography 44
2.19 The different regions that are probed in Laue and Bragg geometry. 45
2.20 A schematic illustration of the formation of the orientation contrast. Note the local differences on the diffracted intensity and consequently to the image on the detector. In (a), the misorientation is larger than beam divergence and wavelength spread (e.g. parallel monochromatic beam) and in (b), the misorientation is smaller than beam divergence (e.g. polychromatic or divergent beam). 46
2.21 A schematic illustration of the formation of the diffraction contrast, formation of the three types of image around a defect: direct (1), dynamical (2) and intermediate image (3) 48

3.1 A schematic diagram showing the geometrical resolution limit set by the projected source height normal to the incident plane. 52
3.2 Non-dispersive setting (+n,-n) setting. The two crystals are identical and the same reflection is used on both. The diffraction vectors are anti-parallel. 53

3.3 Parameters for an asymmetric reflection with Bragg angle θ_B on the diamond sample. All crystal surfaces were along the $< 001 >$ direction. θ_{cut} is the angle between the scattering crystal-planes and the $< 001 >$ surface. 56

4.1 Statistical distribution of rocking curve width broadening for three types of HPHT synthetic diamond material. 60

4.2 X-ray white beam topograph $[\bar{2}20]$ reflection of a type IIa diamond plate. 61

4.3 (a) A zoomed image of one of the stacking faults in figure 4.2 along the indicated undistorted reciprocal lattice vector h and (b) a schematic side view of a dislocation 62

4.4 (a) A zoomed image of the inclusion in figure 4.2, where $\vec{h}$ is the undistorted reciprocal lattice vector and (b) is a geometrical method of estimating distortions due to an inclusion. . . 65

4.5 A perspective view of growth sector boundaries between two different growth sectors with different nitrogen(N) concentrations. 66

4.6 Different growth sectors in a Ib type diamond (white beam, Laue geometry [040] reflection), where $\vec{h}$ is the undistorted reciprocal lattice vector. 66

4.7 Schematic illustration of the formation of equal thickness fringes in a wedge-shaped crystal 67

4.8 (a) A zoom of the equal thickness fringes showed from the top right corner of figure 4.2 and (b) a profile plot of the different intensities on the image using the XOP program (right) . . . 68

4.9 A perspective view of a screw and edge dislocations. The dislocation line $\bar{l}$ and the dislocation Burgers vector $\bar{b}$ have been indicated in each case. 70
4.10 A zoomed portion of the dislocation image from figure 4.2 right hand side. The black line is the direct image and the brighter shadow is the dynamical image. 71
4.11 A schematic illustration of the atomic displacement parallel to the Bragg planes and perpendicular to the diffraction vector g. The Bragg reflection will not be influenced by displacement of atoms perpendicular to the diffraction vector. 73
4.12 Three white beam topographs of a type Ib diamond plate with [100] orientation taken in transmission geometry, with a) Growth sector boundaries, b) dislocations, c) surface scratch and d) growth striations. The arrows indicate the diffraction vector along the direction of the undistorted reciprocal lattice vector h. 73
4.13 White beam topographs of sample 1-3 (HPHT synthetic type IIa diamond samples). The labels (a), (b) and (c) are the [040], [220] and [$\bar{2}$20] reflections respectively. All three samples have central cubic regions generally free of defects detectable through the white beam topography. These samples will later be analyzed through a more sensitive plane and monochromatic wave technique to illuminate the strain fields in the cubic growth sector region 76

4.14 A comparison of the three topographs . Figure (a)⟶ (c) left to right, comparing (a) white beam topograph, (b) and (c) are two double crystal topographs of the same sample taken with different strain sensitivities. 77
4.15 A schematic illustration of the slope of the working point on the steepest linear flank of the rocking curve. The working point has been indicated as a small dot on the left flank 80
4.16 The digitisation process of the topographs. An incident light I_0^L is shone on a film and the transmitted light I^L through the film is collected on a CCD camera. The darker the film, the greater the absorption of light by the film and hence less light will be collected by camera. 81
4.17 The normalised double crystal rocking curves for (a) silicon [444] and diamond [$\bar{1}$15] at 12 keV, (b) silicon [444] and diamond [$\bar{1}$15] at 16 keV, and (c) silicon [800] and diamond [800] at 20 keV respectively. These reflectivity curves were simulated using the XOP software. 85
4.18 The slopes (derivatives) of the rocking curves in figure 4.17 above, namely; (a) silicon [444] and diamond [-115] at 12 keV, (b) Si [444] and diamond [$\bar{1}$15] at 16 keV and (c) silicon [800] and diamond [800] at 20 keV respectively. 86
4.19 Sample 1 – A double crystal rocking curve of the silicon [800] and diamond [800] reflections at 20 keV. Higher order reflections and energy has been used to improve the strain sensitivity. 88
4.20 Sample 2 – A double crystal rocking curve of the silicon [800] and diamond [800] reflections at 20 keV. Higher order reflections and energy has been used to improve the strain sensitivity. 89

4.21 Sample 3 – A double crystal rocking curve of the [444] reflection of the silicon monochromator crystal and the [$\bar{1}$15] reflection of the diamond sample at 12 keV. 90
4.22 Sample 3 – A double crystal rocking curve of the [444] reflection of the silicon monochromator crystal and the [$\bar{1}$15] reflection of the diamond sample at 16 keV. The energy has been increased from 12 keV in figure 4.21 to 16 keV to improve the sensitivity. 91
4.23 A portion of the gray scale values obtained by conversion from the bitmap topographs using the image magic software. . . . 93
4.24 Correction of the non-uniform background illumination. (a) a 2D histogram of the image from the gray scale values, (b) a strip of six pixels broad taken on the boundary edge of the image away from the topograph and averaged to form the boundary values for each of the four sides, (c) a reconstruction of the entire non-uniform background illumination by solving the Laplace problem for the interior points using the illumination at the boundary points and (d) a square histogram with corrected background illumination. 95
4.25 Sample 1 : A quantified topograph of the [800] diamond reflection at 20 keV. The [800] silicon monochromator crystal reflection was used in a double crystal setup. The y-scale in the bottom image was slightly altered (zoomed in) to focus more on the weaker strain fields. The strain sensitivity is in the order of 10^8. 96

4.26 Sample 2 : A calibrated topograph of the diamond [800] reflection taken with the silicon [800] reflection at 20 keV. The y-scale of the bottom image has been slightly altered (zoomed in) to focus more on the weaker strain fields. The strain sensitivity is in the order of 10^{-8}. 97

4.27 Sample 3 : A quantified topograph of a diamond [$\bar{1}$15] reflection taken with the silicon monochromator crystal 444-reflection at 12 keV. The y-scale of the bottom image has been slightly altered (zoomed in) to focus more on the weaker strain fields. 98

4.28 Sample 3 : A calibrated topograph of the diamond [$\bar{1}$15] reflection taken with the [444] reflection of the silicon monochromator crystal in a double crystal setup at 16 keV. The energy has been increased from 12 keV to 16 keV to slightly improve the strain sensitivity. 99

A.1 A portion of the C++ code used for the quantification of the plane and monochromatic plane topographs. 113

List of Tables

1.1 The largest third-generation synchrotron radiation sources present in the world today. 6

2.1 Comparative Figure of Merit (FoM) for diamond, silicon and germanium. 13

3.1 A summary of the experimental setup for the plane and monochromatic wave topography 57

4.1 Rocking curve broadening results for type IIa HPHT diamonds specimens. The theoretical widths were calculated using the XOP software package. 60

4.2 Maximum slopes of the double crystal rocking curves in figure 4.17 above. 87

4.3 Plane and monochromatic wave topographs taken at the working point on the steepest linear flanks of the double crystal rocking curves in figure 4.19–4.22. 92

Chapter 1

Introduction

1.1 Low strain diamond

This study uses x-ray characterisation experiments to understand material science issues at the current extremes of high purity and low strain in synthetic type IIa HPHT diamond. This type of diamond has impurities below 10ppb and large areas where the *effective misorientation* (the deviation of the local Bragg angle in the deformed parts of the crystal from the one in the perfect region) of the lattice in the region of 10^{-8}. The first goal was therefore to characterise the type IIa HPHT synthetic diamonds in this limit of high purity and low strain, and understand the nature of the defects and their contribution to long range strains. It has emerged that this is a non-trivial task, and will necessitate the deployment of x-ray techniques which are extremely sensitive. This research offers a unique opportunity to understand diamond material science in the realm of low strain crystals. It is envisaged that the essential simplicity of the defects and the purity of the material will enable reproducible experiments which are tractable to theoretical interpretation. This has long been a goal of diamond physics.

The primary characterisation tools are x-ray analytical methods appropriate for large single crystals using the brilliant x-ray beams available at the European Synchrotron Radiation Facility (ESRF). The main experimental technique to be used in this research will be the plane monochromatic wave (non-dispersive double crystal) x-ray topography. This research shall, however, employ various other characterisation methods such as the white beam x-ray topography, rocking curve mapping, surface analytical methods including grazing incidence diffraction and specular reflectivity (GID, SAXS, and GISAXS) coherence preservation measurements. These studies are carried out together with conventional spectroscopies such as UV fluorescence imaging, ESR analysis and Raman spectroscopy.

The initial characterisation of this material has revealed a strong correlation of the relative concentration of the impurities with growth sectors. Different growth sectors have different uptake rates of impurities (mainly nitrogen and boron). The average growth rates within different growth sectors may be very uniform but nonetheless different growth sectors proceed at different rates [1]. As a result, the fastest growing sectors grow out first, leaving the slowest growing sectors dominating. There is a correlation between dislocations and stacking faults with different sectors, which also have different (albeit very low) relative concentrations of boron and nitrogen. For the high quality, high purity diamond, the strain appeared very low and uniform in the cubic growth sector.

1.2 Synchrotron-generated x-rays

Synchrotron light is the name given to light radiated by an electric charge moving at a speed close to the speed of light in a curved trajectory. Synchrotron radiation exists in nature (e.g. from the Crab Nebula in which light was observed about 1000 years ago in China during the supernova explosion), but was only given a name later after it was discovered in the laboratory. It is based on the principle that charged particles always emit electromagnetic radiation whenever they are accelerated. The first synchrotron radiation observed in an accelerator was in 1947 at the General Electric Laboratory (NY), where the vacuum chamber was made of glass. In this case, synchrotron radiation light due to electrons in a curved trajectory in the dipole bending magnet was observed. In the late 1960s, a growing number of scientists, mainly physicists, made parasitic use of synchrotron beams extracted out of particle accelerators. These facilities were named first-generation sources [2].

The first synchrotron sources fully dedicated to the production of x-rays and no longer used for particle physics, were called second-generation sources. These first appeared in the early 1980s. In order to increase the flux of the emitted radiation, periodic magnetic structures were soon introduced along the straight sections of the electron or positron storage rings. These insertion devices were named "wigglers" if their magnetic field was so strong that the induced excursion of the particles exceeded the natural opening angle of the synchrotron radiation. For smaller fields and deviations, these devices were named undulators. Many storage rings were equipped with such devices and then dedicated to synchrotron radiation production [3].

Third-generation sources that are optimised to use insertion devices, principally undulators, arrived in the 1990s. A high energy synchrotron radiation facility is regarded as a facility that has more than 5 GeV electron (or positron) energy. Table 1.1 shows the four biggest third-generation synchrotron radiation sources in the world today namely; ESRF, APS, SPring 8 and PETRA III [4].

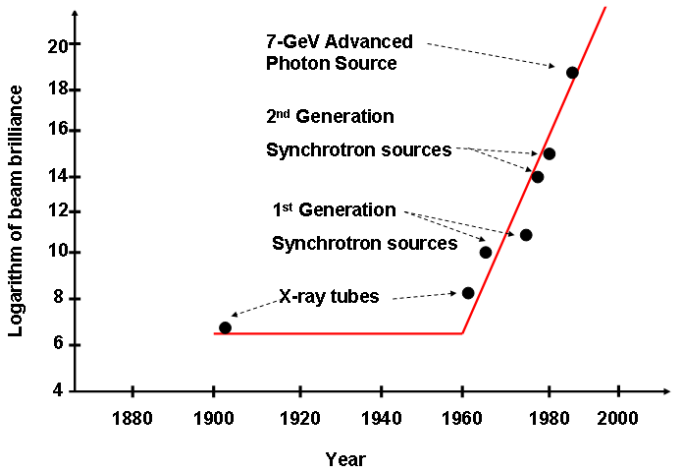

Figure 1.1: Trends in x-ray brightness in various synchrotron sources.

The race to develop a new generation of synchrotron radiation sources with vastly enhanced performance has already begun, even as the third-generation facilities enter their prime, which takes us past the present into the future; namely, to the fourth-generation. The candidate with the best scientific case for a fourth-generation source is the hard x-ray (wavelength less than 1 Å) free-electron laser (FEL) based on a very long undulator in a high-energy electron linear accelerator. Such a device would have a peak brightness many orders of magnitude beyond that of third-generation sources, pulse lengths of 100fs or shorter, and would be fully coherent. Research and development on various technical challenges are well under way at many laborato-

ries around the world. In the United States, efforts are centered around the multi-institutional "Linac Coherent Light Source" proposal to use 15 GeV electrons from the SLAC LINAC as the source for a 1.5 Å FEL, which, if successful, would lay the foundation for a later sub-angstrom x-ray FEL.

In Europe, HASYLAB at DESY is hosting the two-phase TTF-FEL project culminating in a device operating at 6.4 Å several years from now (see progress plan in figure 1.2) [5]. The project will pave the way to a still more ambitious 0.1 Å FEL (TESLA-FEL) further in the future [6].

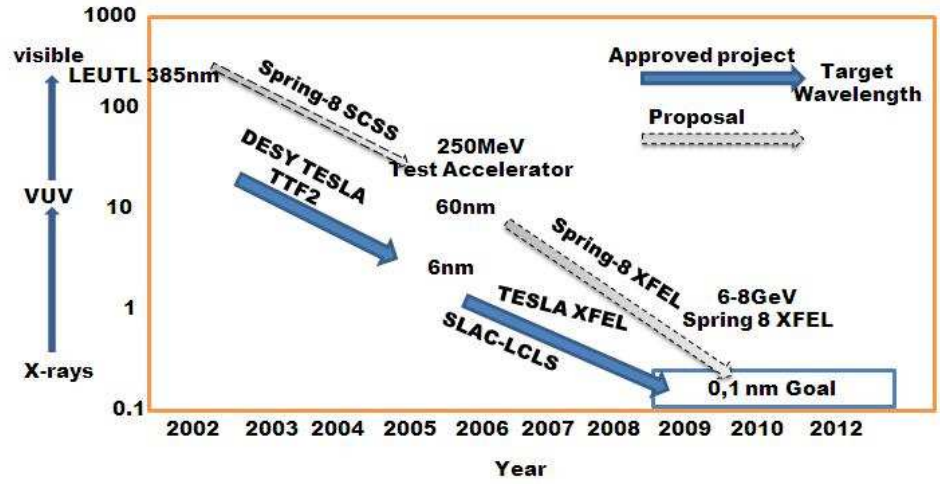

Figure 1.2: Milestones of the SCSS.

In Japan SPring-8, a high peak-brilliance soft x-ray free electron laser project for research and development known as the SPring-8 Compact SASE Source (SCSS), is currently underway. SCSS will be an angstrom x-ray laser facility and shall provide six orders of magnitude peak-brilliance (photons/s/mrad^2/ mm^2/0.1% bandwidth) enhancement compared to the current third-generation sources at 3∼20 nm range.

Name of Facility	ESRF	APS	SPring 8	PETRA III
Constructed by	16 European Countries	US Dept. of Energy	JAERI& RIKEN	German Gov. & Hamburg
Operated by	ESRF	ANL	JASRI	DESY
Location	Grenoble France	Argonne, US	Harima Science Japan	Hamburg Bahrenfeld
Electron Energy	6 GeV	7 Gev	8 Gev	6 GeV
Number of Beam lines	56	68	62	14
Storage Ring Circumference	844 m	1104 m	1436 m	2304 m
Planning	1986-1987	1986-1988	1987-1989	2002-2005
Construction	1988-1994	1989-1994	1991-1997	2007-2008
Operation	1994	1996	1997	2009

Table 1.1: The largest third-generation synchrotron radiation sources present in the world today.

1.3 X-ray Bragg diffraction topography

X-ray Bragg diffraction topography (XRDT) is an x-ray imaging technique that provides two dimensional intensity mapping of the beam(s) diffracted by a crystal. A *topograph* represents a two-dimensional spatial intensity mapping of diffracted x-rays, (i.e. the spatial fine structure of a Bragg spot). The technique records the distortion fields and/or strain fields associated with a macroscopic crystal deformation. This intensity mapping reflects the distribution of scattering power inside the crystal revealing the irregularities in a non-ideal crystal lattice [7]. These variations have their origin in distortions related to the presence of defects, domains, phases, etc. which can in this way, be visualized. The basic principle of x-ray diffraction topography is illustrated in figure 1.3 [8]. Possible extended defects in diamond have been listed in figure 1.4 below. It should be noted x-ray Bragg diffraction topography is not sensitive to individual point defects but the strain fields they cause on the crystal lattice.

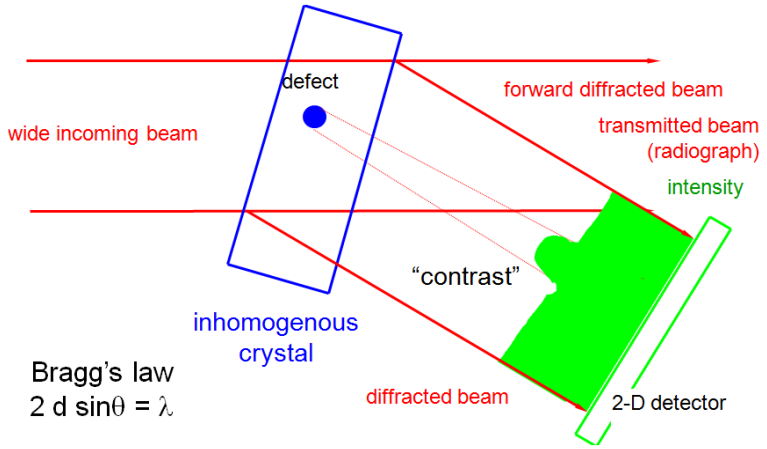

Figure 1.3: Visualization of defects using x-ray diffraction topography.

X-ray diffraction topography is one variant of x-ray imaging, making use of

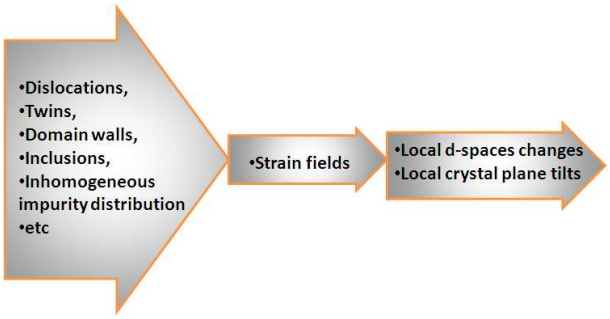

Figure 1.4: Possible extended defects in diamond.

diffraction contrast rather than absorption contrast which is usually used in radiography and computed tomography(CT). XRDT is used for monitoring crystal quality and visualising defects in many different crystalline materials. It has proved helpful (e.g. when developing new crystal growth methods, for monitoring growth and the crystal quality achieved, and for iteratively optimizing growth conditions). In many cases, topography can be applied without preparing or otherwise damaging the sample. XRDT is therefore one variant of non-destructive testing [9].

Modern methods for imaging defects in single crystals using Bragg diffraction (topographic methods) were pioneered more than a century ago by Andrew Lang [6] on the basis of laboratory x-ray generators and only gained momentum in the late 1950's and 1960's due to the developments in the fields of electronics, microelectronics, optoelectronics and crystal growth techniques. Around the 1980's, two developments resulted in the field of high-resolution diffractometry. These were the high intensities at the synchrotron radiation sources and new techniques of x-ray scattering. Silicon (Si) became largely preferred as a material for x-ray optical elements because of its attainability in larger crystals of highest quality. A suitable x-ray optical element for

x-ray Bragg diffraction topography needs to be free from defects such as dislocations, grain boundaries, stacking faults, twins, genuine mosaic structure, near-surface defects and impurity concentration inhomogeneities, which may cause distortion fields in the crystal lattice.

1.4 X-ray optical elements for third and fourth-generation synchrotron radiation sources

The trend in synchrotron radiation (x-rays) is towards higher-brilliance. This may lead to a very high power density, of the order of hundreds of watts per square millimeter at the x-ray optical elements. These elements are typically, windows, polarisers, filters, monochromators and beam splitters [10]. The preferred material at present is silicon, which can be grown to very high crystal perfection and workable size as well as being rather easily processed to the required surface quality. This allows optical elements to be built with a sufficient degree of lattice perfection and crystal processing that they may preserve transversal coherence in the x-ray beam [11]. This is important for the new techniques which include phase sensitive imaging experiments like holo-tomography, x-ray photon correlation spectroscopy, coherent diffraction imaging and nano-focusing. The particular x-ray optical elements that storage rings are equipped with, are briefly described below respectively;

- Windows

  An electron beam with a narrow diameter goes through various components of the storage ring before x-rays derived from it are directed to the experimental beam lines. The vacuum in the storage ring has to be kept very high. Few beam lines work under high vacuum conditions where the low pressure is maintained up to the sample point. In

most cases there have to be transitions from ultra high to low vacuum and to atmospheric pressure. These transitions can be achieved by two methods, one being differential pumping and the other being vacuum windows. The vacuum windows are currently made from beryllium, which has low absorption and is mechanically stable [12]. Sometimes a low (ordinary) quality diamond is also used. For the higher quality x-ray beams, the windows must be homogeneous (bulk) with no voids or density fluctuations, and have a very good surface. Diamond has a low atomic number "Z", like beryllium, and therefore also has a low x-ray absorption.

- Monochromators

  Monochromators are generally used for choosing a narrow energy band of energy wavelengths from the x-ray beam. The monochromation process is based on the principle of Bragg diffraction. Monochromators with perfect lattice materials are needed, like silicon and in the near future, like diamond [13].

- Beam Splitters

  Beam splitters are used to extract a beam with a narrow energy band (monochromatic beam) from a white x-ray beam (by Bragg reflection) to send it to a different experimental station while the transmitted beam can be re-used. Beam splitters are therefore also monochromators [14]. It is possible to extract successively several monochromatic beams (having different wavelengths) from the same white beam. Because the transmitted beam will be used again down-stream, the absorption in beam splitter materials should be kept minimal. It is for this reason that diamond is seen as the best material for this purpose.

- Phase plates

  Perfect single crystals have proven to be effective x-ray retarders. X-ray birefringence occurs in perfect crystals which are oriented in the vicinity (though far away compared to the width of the rocking curve) of Bragg reflection, giving phase shifts between $\sigma - \pi$ polarisation components of the beam propagating through the crystal [15]. In this way the polarisation state of the x-ray beam can be modified [16].

- Filters

  Filters remove the low energy component of a broad spectrum by energy differential absorption, so-called beam hardening.

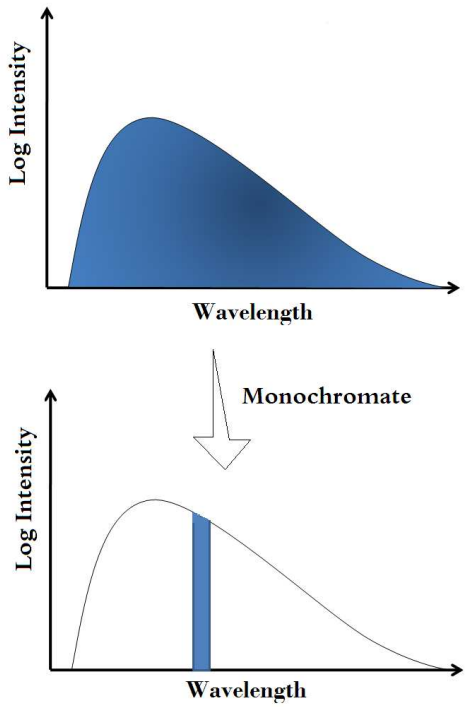

Figure 1.5: Basic principle of x-ray monochromators.

Chapter 2

X-ray optical elements

Diamonds have been adapted for many uses because of the material's exceptional physical characteristics. Most notably, the extreme hardness of diamond, its high dispersion index and its high thermal conductivity [17]. These considerations lead to diamonds becoming increasingly widely used in various applications ranging from jewelery to heat spreaders. Diamonds have many other extreme properties which suggest it for a new range of high tech applications, like optical windows, electronics, single particle quantum devices, and x-ray optical elements for third and fourth-generation x-ray sources (i.e. for synchrotron radiation from storage rings and free electron lasers-FELs).

2.1 Diamond x-ray optics

As indicated previously in figure 1.1, the trend in synchrotron radiation (x-rays) is towards higher brilliance. An appropriate material for optic elements for the future generation x-ray sources needs to have a higher figure of merit, which is defined as follows

$$FOM = 100\kappa/\mu\alpha \tag{2.1}$$

where μ is the linear x-ray absorption coefficient, α is the thermal expansion coefficient and κ is the heat conductivity. Comparative figures of merit for diamond, silicon and germanium are shown in table 2.1 [18].

Temperature(K)	77	300
Diamond	1200	333
Silicon	20	0.47
Germanium	0.66	0.028

Table 2.1: Comparative Figure of Merit (FoM) for diamond, silicon and germanium.

Diamond has a lower absorption coefficient than silicon, a better thermal conductivity and lower thermal expansion coefficient, which would make it the preferred advantageous material in the x-ray optics field [19]. Up to now, synthetic HPHT-grown (high pressure, high temperature) type Ib material have been used in x-ray optics (e.g. as beam splitter monochromators). When propagation distances are large, (10 m and more) from the splitter to the sample (and with other x-ray optical elements on the way), then this results in a wave with a strongly deformed wave front arriving at the sample position with considerable losses in the flux density. This material has at

best a rocking curve broadening of several arc seconds across the crystal face (measured in Bragg mode with 14 keV x-ray on a 400 reflection). The type Ib material has therefore only applications in the less demanding roles such as phase plates. However, in a coherence-preserving beam line, where all elements must be of the same high quality, its quality is far from sufficient [20].

Diamond is still not available with similar dimensions, perfection (bulk and surface), and quantity as for example, silicon which is the most currently used x-ray optical element [8]. Despite this fact, diamond is becoming increasingly used in beam lines of third-generation synchrotron sources as monochromators, beam splitters, filters or phase plates/polarizers.

Advances in HPHT synthesis methods have allowed the growth of type IIa diamond crystals of the same size as type Ib, but with substantially lower nitrogen content. More recently, even higher quality HPHT IIa diamonds have been synthesised, where the nitrogen and boron content are each below 10 ppb, and where rocking curve broadening is essentially negligible for the cubic growth sector regions. The thesis addresses itself to this latter material.

2.2 High Pressure High Temperature Synthetic diamonds

2.2.1 Synthesis

The first commercially successful synthetic High Pressure and High Temperature (HPHT) diamond was achieved in Stockholm, Sweden, in 1953. The discovery was kept secret [21]. A year later, General Electrics Research Lab-

oratory reported two other successful synthesis, one of them by H.M. Strong and the other by H.T. Hall. Their method of growing man-made diamond was published in Nature [22]. In 1971, R.H Wentorf Jr. showed the possibility of growing bigger diamond using the so called "*thermal gradient method*".

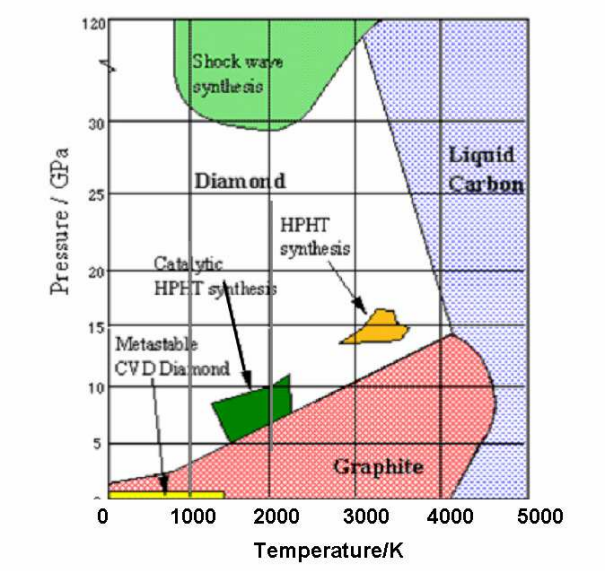

Figure 2.1: A pressure-temperature phase and transformation diagram for carbon .

Our understandings of the pressure-temperature phase and transformation diagram (figure 2.1) for carbon has recently undergone very important advancements [23]. A wide spectrum of complex hybrid forms of carbon and many metastable forms exist due to the high activation energies for solid-state transformations and the specific effects of reaction paths. However, graphite, diamond, liquid and vapour remain the major thermodynamically stable forms of carbon [24]. The four techniques/regions shown in figure 2.1,

namely; the Chemical Vapour Deposition (CVD), shock wave, HPHT direct conversion and HPHT catalyst synthesis of diamond are briefly discussed below

Chemical Vapour Deposition (CVD) growth technique

The CVD growth technique generally involves the growth of a solid material from the gas phase using a reactive gas mixture, which supplies the necessary active species (carbon from methane in the case of diamond) onto a controlled surface (or substrate). The substrate may not necessarily be diamond, however, a diamond substrate with high quality surface finishing is (instead of polycrystalline diamond) required to grow single crystal diamond. CVD growth is the most widely used technique for depositing many materials in the semiconductor industry, including a wide range of dielectrics and many metals and metal alloys. The main advantages of this technique are that equipment used for synthesis is relatively cheap (because it works at relatively low pressures), bigger diamonds can be grown, and diamonds may be grown on different substrates. Unfortunately, until now, the quality of the bulk material does not meet the requirement to be used as x-ray optical element.

Shock wave synthesis

In the shock wave synthesis, detonation is used to produce very high pressure and temperature enabling CO and CH_4 molecules to disproportionate in to diamond, oxygen, hydrogen and hydrocarbons of other composition. The shock wave synthesis produces very tiny diamonds, not suitable for the applications as optical elements [25].

HPHT direct conversion

Although thermodynamically feasible at low pressure and temperature, the transformation of graphite to diamond faces a considerable kinetic barrier since the rate of transformation apparently decreases with increasing pressure [26]. The favourable thermodynamic conditions are superseded by this kinetic consideration, hence very high pressure and temperature (>139 kb and >3300 K) are necessary in order for the direct graphite-diamond transformation to proceed at an observable rate [26].

HPHT catalyst synthesis

In order to pass the kinetic barrier, a metal solvent-catalyst bath is used. This allows the conversion to happen at a lower temperature and pressure, typically around 1550 -1600 K and 5-6 GPa [27]. This is the method used to grow high quality diamond and the attention will be focused on this specific technique.

Alloys of iron and cobalt are used in the solvent-catalyst and additionally, getter components are introduced to the diamond synthesis process due to their high affinity for nitrogen [28]. The getters are selected from those elements which have a stable nitride at high temperatures such as titanium, aluminium and zirconium. The presence of getter components reduces the range of temperatures in which well-formed diamond crystals will grow. When the temperature is too low, precipitation of carbides competes with the resorption of the diamond crystals. If the temperature of growth is too high, the rate of growth is increased to the point where the metal solvent cannot be excluded and the crystal becomes contaminated by metal inclusions. There is therefore a very small temperature range in which good crystals can be

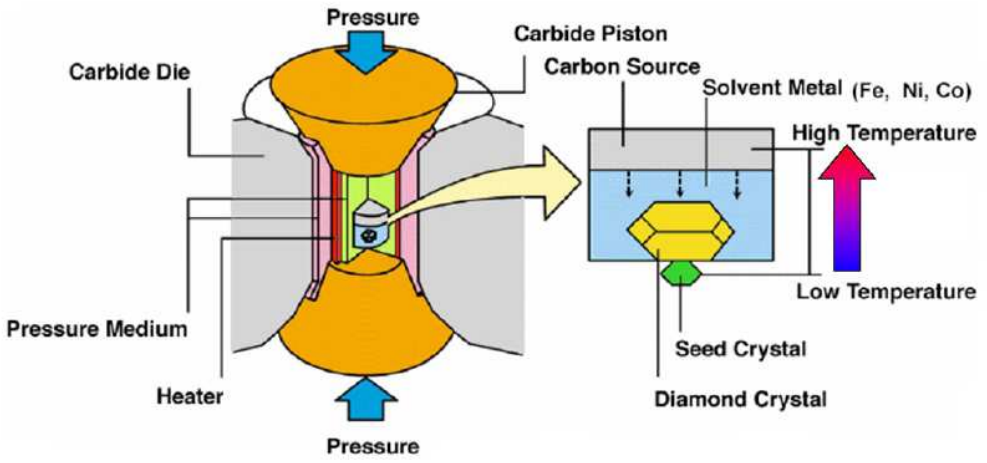

Figure 2.2: A growth mechanism for High Pressure High Temperature (HPHT) synthetic diamonds.

grown which necessitates an appropriate system of temperature control. This growth mechanism has been illustrated in figure 2.2 [29].

The diamond lattice

The diamond crystal is formed by sp^3-bonded carbon atoms arranged in the so-called "diamond lattice", which consists of two inter-penetrating face-centered cubic lattices shifted by a vector (a/4, a/4, a/4). One unit cell of the diamond cubic crystal structure has a lattice parameter of $a = \frac{\sqrt{3}\pi}{16} \approx$ 3,56683 Å and bond length of 1.54 Å at room temperature. The unit cell contains the equivalent of 8 whole C atoms with a packing fraction of approximately 0,34. Each atom can be thought of as a sphere with a radius of 1/8 of the cubic body. The atomic density is therefore $8/{a_0}^3 \approx 8/(3,56683 \times 10^{-10}\text{m})^3 = 1,76 \times 10^{29}$ atoms m^{-3}. A conventional diamond unit cell has been illustrated in figure 2.3 with the lattice parameter a_0 and

the bond length clearly indicated. It is worth mentioning that a hexagonal form (lonsdaleite) is also known, but it is extremely rare.

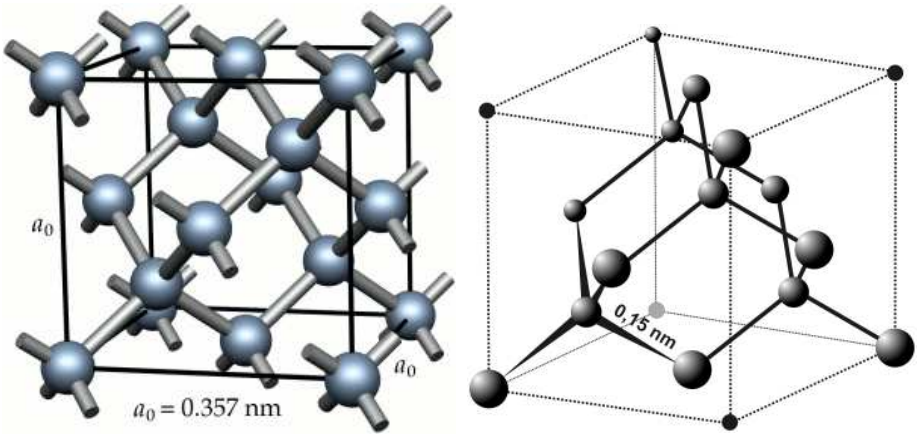

Figure 2.3: Conventional diamond unit cell.

Nitrogen and boron concentrations dependences in different growth sectors in diamond

Synthetic HPHT diamonds usually have a yellow colour, shading into brown in extreme cases because of the presence of a few tens to a few hundreds of parts per million (ppm) of nitrogen which is thought to be derived from both the atmospheric air (pore space) in the materials of the synthesis capsule, and also impurity nitrogen in the solvent catalyst metals. A correlation exists between the nitrogen and boron concentrations with the different growth sectors in diamond [8, 30]. The dependences are as follows for boron and nitrogen, respectively :-

$[111] > [110] > [100] = [113] > [115]$ for boron

$[111] > [100] > [113] > [115] > [110]$ for nitrogen

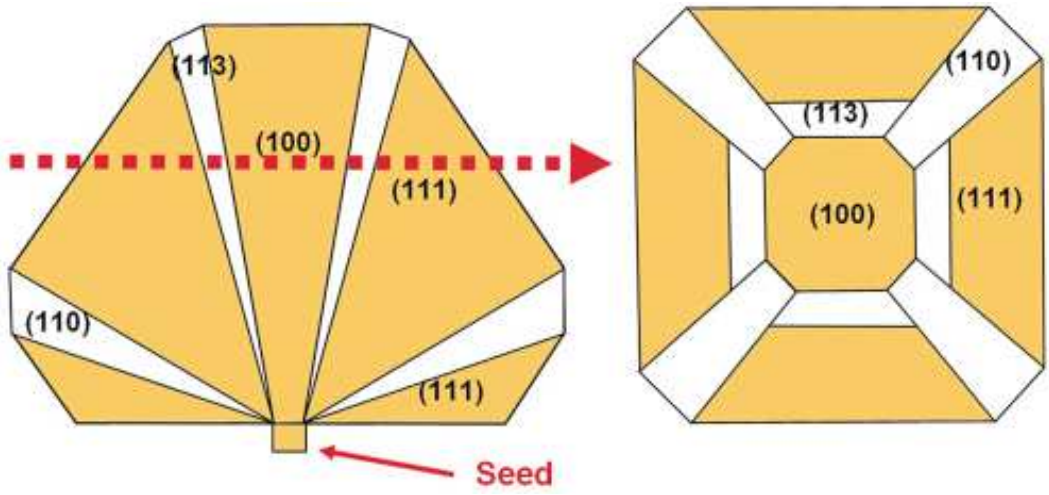

Figure 2.4: Growth sectors seen most frequently in the growth of near cubo-octahedral HPHT diamond crystals of type Ib. The right image is a top view of an extracted plate at the level shown by the dotted line.

The frequently observed growth sectors in the growth of near cubo-octahedral HPHT diamond crystals of type IIb has been illustrated in figure 2.4 with growth face orientations clearly indicated [21]. The image on the right shows a top view after a cut along the dotted arrow to obtain the slice furthest from the seed which has proven to be of best quality.

Figure 2.5 shows UV and x-ray white beam topograph on one of the first type Ib HPHT synthetic diamond samples, which exhibits the nitrogen and boron concentration dependencies on growth sectors. The nitrogen concentration is higher in the brown sectors of the optical image.



Optical image

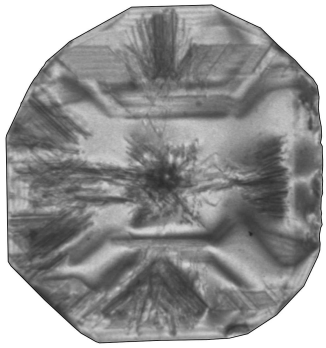

x-ray white beam topograph

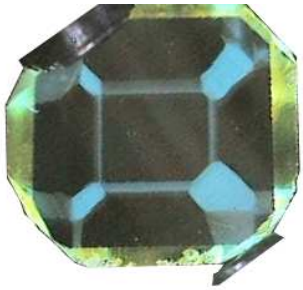

UV image

Figure 2.5: Nitrogen and boron concentration dependencies on growth sectors observed using UV fluorescence and x-ray white beam topograph on one of the first type Ib HPHT synthetic diamond samples

2.2.2 Optical properties

A chemically pure and structurally perfect diamond is perfectly transparent with no hue, or colour. The colour of a diamond may be affected by chemical impurities and/or structural defects in the crystal lattice. HPHT Type IIa diamonds are so far proven to be the lowest strain diamonds. They contain few extrinsic impurities, and may have their colour modified by structural dislocations or plastic deformations. Both natural and synthetic diamonds grown under high pressure and high temperature (HPHT) conditions can be optically classified into different types Ia, Ib, IIa and IIb, depending on the impurity content and distribution. In type Ib diamonds the major impurity is nitrogen, whereas the type IIa diamonds are effectively free of, or very low in nitrogen. Therefore, type Ib diamond crystals are typically yellow in colour, and the variations of yellow colouration due to local variations in nitrogen concentration can be visually discerned in XEOL (x-ray excited optical luminescence) pictures [15].

Prismatic effect

Diamonds exhibit a high dispersion of visible light. This strong ability to split white light into its component colours is an important aspect of diamond's attraction as a gemstone, giving it an impressive prismatic action that results in the so-called *fire* in a well-cut stone. The lustre of a diamond, its adamantine brilliance, is a consequence of its high refractive index of 2.417 (at 589.3 nm), which allows total internal reflection to occur easily [31]. Some diamonds exhibit fluorescence of various colours (predominately blue) under long-wave ultraviolet radiation.

Fluorescence

Any emission of light at temperatures below that required for incandescence is called luminescence. Fluorescence is a luminescence that is mostly found as an optical phenomenon in cold bodies, in which the molecular absorption of a photon triggers the emission of another photon with a longer wavelength. The energy difference between the absorbed and emitted photons ends up as molecular vibrations or heat. Usually the absorbed photon is in the ultraviolet range, and the emitted light is in the visible range, but this depends on the absorbance curve and stokes shift of the particular fluorophore. Fluorescence is named after the mineral fluorite, composed of calcium fluoride, which often exhibits this phenomenon. This is typically a fast process in which some of the original energy is dissipated so that the emitted light photons are of lower energy than those absorbed.

Fluorescence in diamonds

About a third of natural diamonds fluoresce under the ultra violet (UV) light. Fluorescence can be faint to very strong, and the most common fluorescent colour is blue. As blue is the complementary colour to yellow, the most common tinted colour in diamonds, blue fluorescence can make yellowish diamonds look white or colourless. Most diamonds show no fluorescence although coloured diamonds show a wider range of fluorescence than the blue fluorescence normally observed in clear diamonds. However, nearly all diamonds fluoresce bluish-white, yellow, or green under shorter x-ray radiation. X-ray screening is used extensively in mining to separate the diamond-bearing rock with exposed or loose diamonds from the non-fluorescing waste rock.

Phosphorescence

Phosphorescence is a specific type of photoluminescence related to fluorescence. Unlike fluorescence, however, a phosphorescent material does not immediately discharge the radiation it absorbs. The slower time scales of the re-emission of the radiation are associated with quantum mechanically forbidden energy state transitions. The energy is stored in the substance and released very slowly and continuously in the form of light. It is the mechanism used for "glow in the dark" materials which need to be charged up by exposure to light. The probability for the process of emitting light to occur is very low and almost forbidden by quantum mechanics. Therefore, on a microscopic level, the rate of energy release is characteristically slow, and hence the light can glow for several minutes [23].

Phosphorescence in diamonds

When a 222nm ultraviolet light is shone on diamond, excitation occurs. In principle, light energy can be absorbed or emitted from a band-gap semiconductor if an added substance forms an impurity level within the gap.

During exposure to UV light, diamonds sometimes give off a blue, green, orange, yellow or (rarely) red glow (and sometimes "phosphoresce" for a while after exposure). These characteristic colours arise due to the type of impurity. Synthetic diamonds are usually inert in long wave UV ($\sim$ 350 nm). In shortwave ($\sim$ 250 nm) UV light, some glow yellow or yellowish-green. The fluorescence is frequently uneven, with different coloured or inert regions. In addition, colours are usually strongly zoned during fluorescence due to different incorporation of N and B in the different growth sectors. Like boron-containing type IIb diamonds, type IIa diamonds transmit in the ul-

traviolet down to 250 nm. Depending on the type of defect, some defects can be "healed" and the colour removed by treatment with high temperatures and high pressures.

In a blue diamond, a few carbon atoms out of a million have been replaced by boron atoms each containing three valence electrons. The structure of diamond is not significantly perturbed, and the absence of an electron is represented by a partially localised acceptor "hole" state just above the valence band. With the absorption of energy, electrons can be excited from the valence band into the hole acceptor states. The absorption of energy in the longer wavelength region leads to a blue colouring of the diamond. Similarly, in a yellow diamond, a few carbon atoms out of a million have been replaced by nitrogen atoms, each containing five valence electrons. The structure of the diamond is also not significantly perturbed, but the extra electrons enter a "donor level", so called because, with the absorption of energy, these electrons can be donated to the empty conduction band. The resulting absorption at the blue end of the spectrum leads to a yellow colour seen in both natural and synthetic nitrogen-containing diamonds [32].

In diamond, the acceptor and the donor levels are too deep (0.37 eV above the valence band for a boron acceptor and 1.6 eV below the conduction band for the nitrogen donor) in the gap to be significantly ionised at room temperature (0,27 eV). The donor is especially deep below the conduction band. Diamond is a wide band gap (5,6 eV or 228 nm wavelength) semiconductor. Light quanta with any energy above 1.6 eV can excite the extra electrons into the conduction band from the donor band [33]. Blue phosphorescence in pure low strain diamond may occur if an acceptor and a donor are close

to each other physically making it easy for the free electron of the donor to jump into the hole of the acceptor leaving both of them ionised. An electron can then be photo-excited to the compensated donor level.

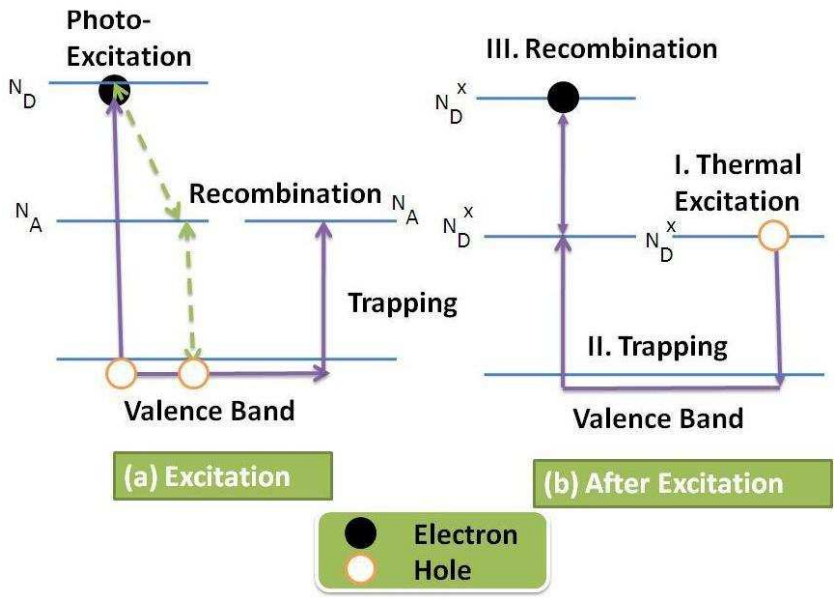

Figure 2.6: Schematic energy level representation of the (absorption band) basic model for phosphorescence in type IIa HPHT diamond.

Figure 2.6 shows the excitation in (a), where an electron is photo-excited to the compensated donor level N_D, leaving a hole in the valence band. Some pairs recombine through donor-acceptor recombination and emit photoluminescence during and shortly after excitation, and others remain apart between holes in an isolated neutral acceptor N_A^{χ} and electrons in a neutral donor N_D^{χ}. After excitation (b) holes are ionised thermally from isolated acceptors in (I), and in (II) trapped by ionized acceptors N_A accompanied by neutral donors, then (III) recombination takes place [33].

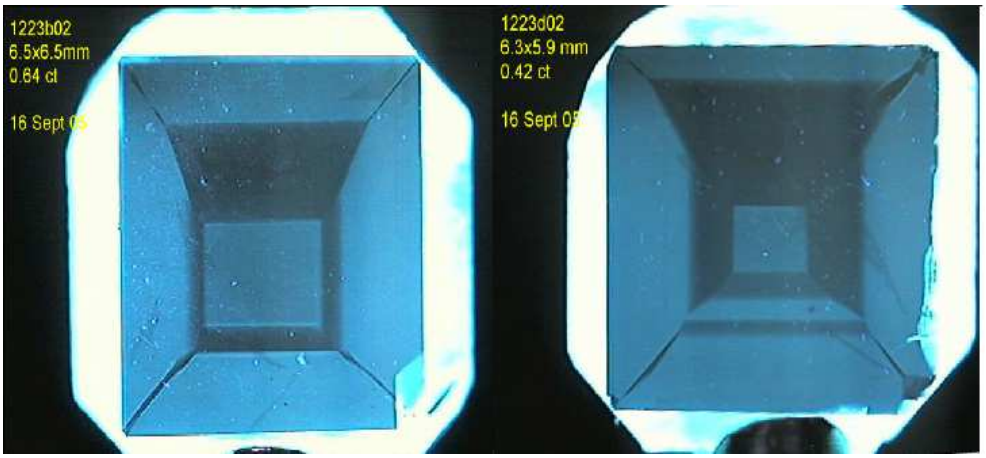

Figure 2.7: Cathodoluminiscence images, revealing a non-uniform nitrogen concentration (C_N) mainly around growth boundaries

The diamonds that are the focus of his work, type IIa HPHT diamonds, typically phosphoresce in the light blue, with a strong sectoral variation. The sectoral variations is due to the different relative concentrations of nitrogen and boron in the different growth sectors as seen for example in figure 2.7. The donor acceptor recombination mechanism and the blue luminescence explained above can be used to understand figure 2.7 [29]. In this figure, the proximity and relative concentrations of the B and N acceptors and donors respectively are important. The black area does not necessarily imply that there is no B and N. It could also be due to over-compensation. For example, the [100] sector has a relatively low B and a relatively high N.

The dependence of the dilatation of the diamond lattice on the P1 nitrogen impurity content is given by Lang's dilatation formula

$$\frac{\triangle a_o}{a_o} = (0.12 \pm 0,03) \times C_N \tag{2.2}$$

where C_N is the nitrogen impurity concentration expressed as an atomic

fraction. In this way, a varying concentration of defects would lead to a varying lattice constant which leads to strain. It is therefore very important for the defect or impurity concentrations to be uniform and minimal.

2.2.3 Thermal properties

Diamond-based elements provide several very advantageous properties, one being its low x-ray absorption due to its very low atomic number and with that its electron density. The low linear x-ray absorption coefficient by comparison with silicon, makes it more suitable for transmission of x-rays through filters, monochromator crystals and beam splitters (the latter used in transmission or Laue geometry) without excessive heating. Diamond is a good conductor of heat because of the strong covalent bonding within the crystal. Specially purified synthetic diamond has the highest thermal conductivity of between $2000 - 2500$ W/(mK), five times more than copper and higher than for any known solid at room temperature. It has the highest thermal conductivity at room temperature.

Because diamond has such high thermal conductivity (κ) it is already used as a heat spreader in semiconductor manufacture to prevent silicon and other semi-conducting materials from overheating. Ultra pure diamond single crystals are the only promising materials for x-ray optical elements to sustain high resolving powers of the future fourth-generation sources [34]. The superior thermal conductivity of diamond and its small thermal expansion coefficient (0.8×10^{-6} K^{-1}) allows the energy deposited in the element to be conducted away to the support mechanism relatively easily without much lattice distortion. This allows for minimal thermal deformation, and so also the resulting x-ray beam deformations, due to the minimised heat load. In figure 2.8, both

the height and the broadness of the two *rocking curves* (containing statistical intensity $I(\theta_B + \delta\theta)$ information on the divergence recorded at a given angle $\delta\theta$ close to the Bragg angle θ_B) are not affected during extreme heat loads of 0.5 W/cm^2 and 1.5W/cm^2 respectively. Therefore, ultra pure diamonds will sustain high resolving power under the extreme heat load conditions of the future synchrotron radiation sources [18].

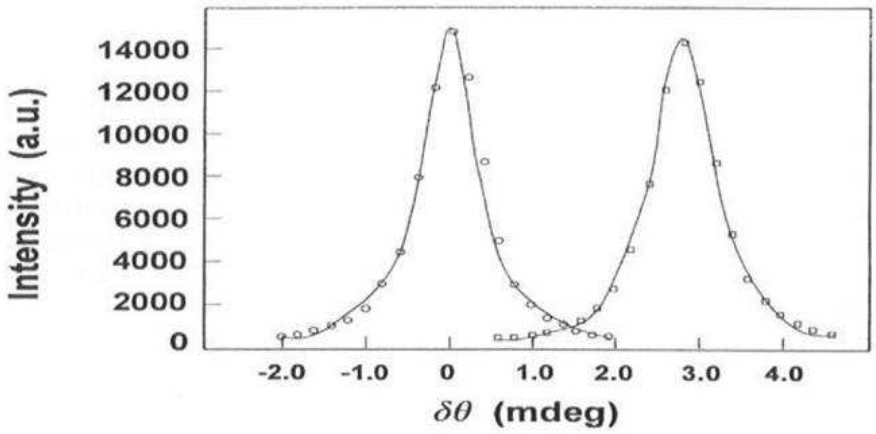

Figure 2.8: Two x-ray rocking curves under two heat loads 0. 5 W/cm^2(left) and 1. 5 W/cm^2(right). A demonstration of excellent thermal properties of diamond suitable for x-ray optical elements for third and forth x-ray generation sources.

2.3 X-ray diffraction(XRD)

2.3.1 Response of a crystal to a plane-wave

When a plane x-ray wave strikes a three-dimensional atomic lattice, it is both scattered and absorbed. Absorption may be described by the usual absorption equation

$$\frac{I_a^x}{I_o^x} = e^{-\mu t} \tag{2.3}$$

which is only applicable to non-Bragg reflecting situations [35]. Here, I_o^x is the incident x-ray beam, I_a^x is the transmitted beam intensity, μ is the linear absorption coefficient and t is the thickness of the specimen in the direction of the x-ray beam [36].

X-ray scattering may be easily understood by considering an x-ray photon incident on a single atom, where the electrons in that atom will oscillate about their mean positions thereby re-emitting x-rays. This process of absorption and re-emission of electromagnetic radiation is known as *scattering*. Using a concept of a photon, one may say that an x-ray photon is absorbed by the atom and another photon is emitted. When there is no change in the energy between the incident photon and the emitted photon,(no energy transfer occurs during the scattering process) the radiation is said to be *elastically* scattered. However, if the energy of the incident photon differs with the energy of the emitted photon, the radiation is said to have been *inelastically* scattered. *Bragg's law* (equation 2.4) provides the condition for a plane-wave to be diffracted by a family of lattice planes as illustrated in figure 2.9 below

$$n\lambda = 2d \sin\theta_B \tag{2.4}$$

where λ is the x-ray wavelength, d is the inter-planar spacing, θ_B is the (Bragg) angle of incidence and of diffraction of the radiation relative to the reflecting plane, and n is an integer known as the *order of reflection* and is the path difference, in terms of the number of wavelengths, between waves

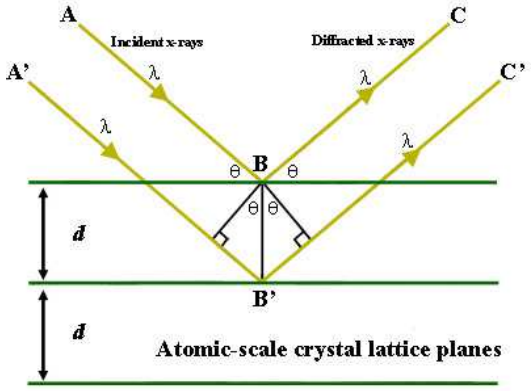

Figure 2.9: A schematic illustration of the Bragg law, $n\lambda = 2d\sin\theta$. An incident plane-wave is diffracted off successive crystal planes.

scattered by adjacent planes of atoms. A first-order reflection occurs when $n = 1$ diffraction and the scattered and the incident waves have a part difference of one wavelength, when $n > 1$, the reflections are called high order. Therefore, Bragg's law (equation 2.4) may be written as

$$\lambda = 2\frac{d}{n}\sin\theta_B = 2d_{hkl}\sin\theta \tag{2.5}$$

where $d_{hkl} = d/n$ is the spacing between the reflecting lattice planes $(nhnknl)$.

The scattering strength of a unit cell for a particular lattice plane reflection, hkl, is known as the *structure factor*, which is explained using equation 2.8. The larger the structure factor, the broader is the rocking curve[37]. The intensity I^x of the x-rays scattered by one electron through an angle 2θ relative to the incident intensity I_o^x is

$$\frac{I^x}{I_o^x} = \frac{C^2 r_e^2}{R^2} \tag{2.6}$$

where R is the distance from the particle and $r_e = \frac{e}{mc^2}$, e is the electronic

charge, m is rest mass of the electron, c is the velocity of light and C is the factor dependent on the polarisation [37].

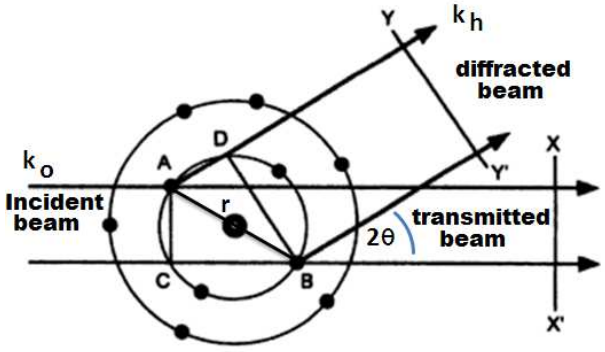

Figure 2.10: Scattering of x-rays by an atom.

Figure 2.10 shows an atom containing several electrons as points around the nucleus [38]. This model is not consistent with the quantum mechanical definition of the atomic structure, however, it helps with the explanation. The two electrons **A** and **B** scatter the two incident waves in the forward direction. The forward scattered waves are in phase across the XX‘ wavefront. The other scattered waves will not be in phase across wavefront YY‘ when the path difference (CB-AD) is not the integral number of wavelengths [38]. The wave vectors $\vec{k_0}$ and $\vec{k_h}$ are in the directions of the incident and diffracted beams, respectively, and $|k_0| = |k_h| = 1/\lambda$. The phase difference will be given by

$$exp[-2\pi ik.r] = exp[-2\pi i(hu + kv + lw)] \tag{2.7}$$

for the *hkl* reflection, where *(uvw)* are the fractional coordinates of the vector **r**. The waves scattered from each atom may now be added with regards to the atomic scattering factor of each atom and the phase of the wave from each atom summed up over the unit cell.

$$F_{hkl} = \sum_i f_i exp[-2\pi i(hu + kv + lw)] \tag{2.8}$$

with f_i being the atomic scattering factors of the atoms of type i. These depends on both θ and λ. Generally small-angle elastic scattering is coherent, while inelastic scattering is incoherent. Large-angle elastic scattering becomes rapidly more incoherent with increasing scattering angle.

Kinematical Theory of x-ray diffraction

Kinematical theory evolved from the geometrical theory to account for diffracted intensity from a real crystal under the following conditions [39];

- the x-rays scattered by atoms and lattice points of the crystals are coherent and elastic,
- the interactions between the scattered x-ray photons and the nuclei is ignored,
- both the incident and the scattered waves are considered to be plane-waves and
- multiple scattering effects are negligibly small and the scattered waves are not subject to scattering from other atoms and lattice points.

The kinematical theory assumes that a negligible amount of energy is transfered to the diffracted beam, with the consequence that the re-diffraction effects may be we ignored . For example, the weakening of the incident wave by the scattering process (*extinction*) is ignored, and every part of the crystal is assumed to be illuminated with the same incident intensity. Although disregarding extinction obviously violates the law of conservation of energy, kinematical theory is fairly accurate for the geometry of diffraction in all

cases, and reasonably enough, it is also fairly accurate for intensities when the scattering is very weak. When the scattering is strong (e.g. diffracted intensities and rocking curve widths for near perfect crystals), this assumption is hopeless [37].

2.3.2 Dynamical theory of x-ray diffraction

As mentioned in above in section 2.3.1, the kinematical theory (although very useful for crystal structure analysis) is unsatisfactory in predicting diffracted intensities of anything other than very thin or very small crystallites. As crystal thickness increases, the kinematical theory is unable to explain a saturation in intensity caused by the presence of strong wave fields from dynamical diffraction effects.

A suitable theory to describe the diffracted intensities in all kinds of crystals is *dynamical diffraction theory*, which will be briefly introduced in this section. Several versions of the dynamical diffraction theory exist for perfect and imperfect crystals. The theory for "thin" and much distorted crystals are rather different. We aim not to derive any such formulations of the dynamical diffraction theory, but to mention parts of it which shall be used in this research, especially, the strong approximation of the dynamical diffraction theory of perfect crystals for distorted ones.

The interaction of incident waves with the diffraction wave was first considered by Darwin(1914) [40, 41], and then modified by Prins and Kohler(1930) by taking crystal absorptions into account. A different dynamical theory (with a wider scope than Darwin's) was investigated P.P. Ewald (1916/17)

dealing with the interactions of electromagnetic fields with three-dimensional array of dipoles. In 1931, M.Laue reformulated the dynamical theory based on solutions of the Maxwell's equation for interactions of x-rays with crystals by treating the crystal as a medium with a periodic complex dielectric constant[42]. Laue's treatment of the dynamical theory has been frequently used in the literature due to its simpler mathematical form [43]. In general, the dynamical diffraction theory aims to solve the following inhomogeneous wave equation

$$\varphi(r) = \varphi_o(r) + \int\int\int G(r \mid \acute{r})V(\acute{r})\varphi(\acute{r})d^3\acute{r} \tag{2.9}$$

where $\varphi_o(r)$ is the solution of the homogeneous equation and $\int\int\int G(r \mid \acute{r})V(\acute{r})d^3\acute{r}$ is the solution of the inhomogeneous equation with $V(\acute{r})\varphi(r)d^3\acute{r}$ being the inhomogeneity of the equation. G and V are the lattice amplitude factor and the volume of the crystal unit cell respectfully .

Effects of multiple scattering process (diffraction and re-diffraction)

The process of diffraction and re-diffraction of an x-ray beam from a set of reflecting planes is illustrated in figure 2.11 in Laue case. As the incident wave propagates down into the crystal, its amplitude diminishes since a small fraction of the energy is reflected at each atomic plane.

Under both transmission (Laue) and reflection (Bragg) geometries (see section 2.5.2), the incoming beam fulfills the Bragg condition and the two diffracted beams are created. In the reflection geometry, the two wave fields are strongly damped in depth until extinction is reached and one wave field may be ignored.

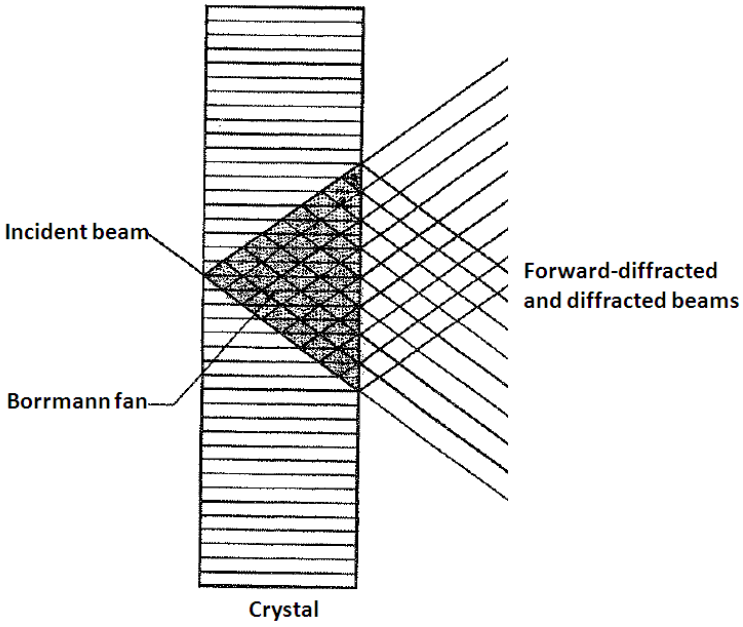

Figure 2.11: The diffraction and re-diffraction of an x-ray beam from a set of reflecting planes in Laue case.

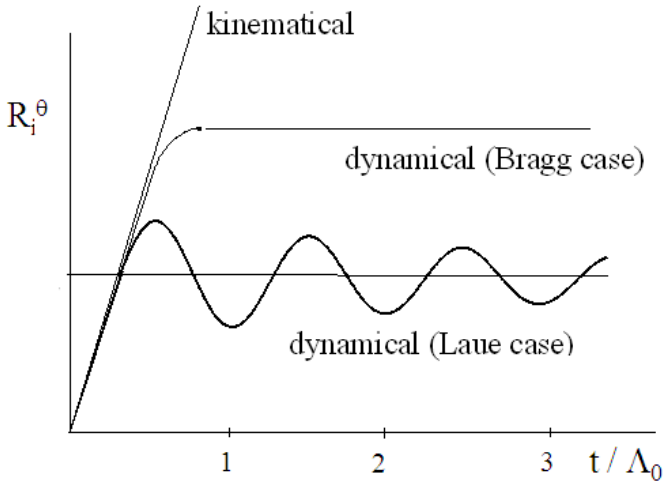

Figure 2.12: Integrated intensity (reflectivity) as a function of thickness as described for non-absorbing crystals by kinematical and dynamical theories

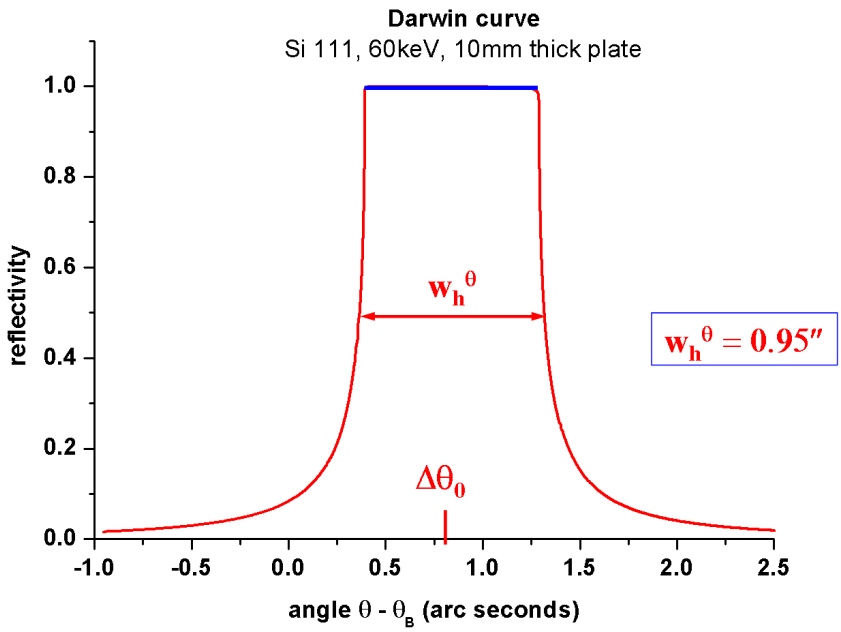

Figure 2.13: An example of a reflectivity curve (known as the Darwin curve) of a thick non-absorbing silicon crystal [111] Bragg reflection. The region with R=1 is flat (top had shape) due to *interference total reflection* and the maximum of the reflectivity curve is shifted by the refraction correction $\Delta\theta_0$. The curve has been calculated using the XOP simulation software package.

Figure 2.13 shows a reflectivity curve of a 111 reflection of a 10 mm thick silicon crystal thick plate with a "top hat"(flat top) shaped reflectivity curve due to *interference total reflection*–the so called Darwin Plateau. Without considering any absorption, the reflectivity curve is symmetric, and is equal to 1 in the range $(\triangle\theta_o - w_h^\theta/2) - (\triangle\theta_o + w_h^\theta/2)$. Where $\triangle\theta_o$ is the angular displacement of the reflectivity curve "R" with respect to the Bragg angle θ_B and w_h^θ is the full width at half maximum of the reflection curve, which is given by

$$w_h^\theta = \frac{2d_{hkl}}{\wedge_o}\frac{\mid \gamma_h \mid}{\cos\theta_B} \tag{2.10}$$

In Laue geometry, the damping of wave fields in depth is not strong, but contrary, there may be anomalously weak damping in depth of thick crystals ($\mu t >> 1$)–anomalously strong transmission (*Borrman effect*). The intensity of x-rays is shuffled from the forward diffracted beam into the Bragg diffracted beam. This round-trip period is called the *Pendellösung length* $\wedge_o$ and it can be used to define how "small" (thin with $A << 1$) or "large" (thick with $A >> 1$) a crystal is, as illustrated by equations 2.11 and 2.12 below;

$$A = \pi t/\wedge_o \tag{2.11}$$

$$\Lambda_o = \frac{\sqrt{\gamma_o \mid \gamma_h \mid}}{K \mid P \mid \sqrt{\chi_h \chi_{\bar{h}}}} \tag{2.12}$$

where $K = 1/\lambda$ is the wave number in vacuum, P = polarisation factor, χ_h and $\chi_{\bar{h}}$ are the Fourier components of the elastic susceptibility and γ_o and γ_h are the direction cosines.

Figure 2.12 compares the integrated intensity (reflectivity) defined by equation 2.13, as a function of thickness as described by kinematical and dynam-

ical theories. The integrated intensity, R_i^θ is given by

$$R_i^\theta = \int R_h(\theta) d\theta \tag{2.13}$$

For a non-absorbing thin crystal (kinematical limit), kinematical and dynamical values are the same, and both Laue and Bragg case reflectivities are the same and are given by equation 2.14 below,

$$R_{i(thin)}^\theta = \frac{\pi^2 \mid P \mid^2 K(\chi_h^e \chi_{\bar{h}}^e) t}{\gamma_0 \sin\theta_B} \approx V \mid F_h \mid \tag{2.14}$$

It is seen that kinematic theory diverges drastically at larger thickness. In Laue case, the dynamical theory oscillates about a saturated level after a thickness of about $\wedge_o$ [37]. In Laue case, the integrated intensity R_{iL}^θ is given by

$$R_{iL}^\theta = \frac{\pi \mid P \mid \sqrt{(\chi_h^e \chi_{\bar{h}}^e)}}{2\sqrt{\mid b \mid} \sin\theta_B} \approx \mid F_h \mid \tag{2.15}$$

the average of which is half that of Bragg case (i.e. $R_{iB}^\theta = 2R_{iL}^\theta$).

2.4 Local rocking curve measurements

X-ray rocking curves measurements are commonly used for characterising the perfection of crystalline samples. Silicon and diamond reflectivity curves were calculated using the XOP software (obtained from [44]) and presented in figure 2.14. A double crystal rocking curves is a convolution of the crystal reflectivity curve with an apparatus or instrumental function (i.e. both angular and wavelength spread created by the source and all the optical elements).

Often the full width at half maximum (FWHM) of a rocking curve is extracted as a very compact integral measure of the crystal quality. Crystal lattice strain can be measured from an increase of the FWHM relative to

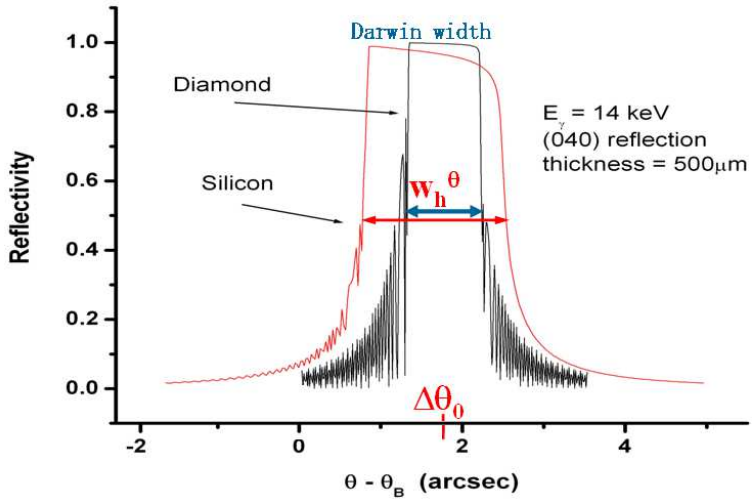

Figure 2.14: Reflectivity curves for silicon and diamond. The full width at half maximum w_h^θ for the two curves is illustrated in both curves. The reflectivity curves were calculated using XOP software from ESRF.

the value of a perfect crystal. These variations may, for example, result from variations of impurity concentration concentrations, dislocation concentrations, temperature fields (e.g. heat bump), or some other sources of strains. Estimation of the influence of the FWHM is an objective of big practical importance in the diamond for x-ray optics project.

2.5 X-ray Bragg diffraction imaging (topography)

As previously introduced in chapter 1, x-ray diffraction topography is an imaging technique that uses x-ray beams that have been Bragg diffracted by a crystal to provide a two-dimensional intensity mapping (known as a topograph) of the beam(s) diffracted by a crystal. Topography is not sensitive to individual point defects but to the long range distortion fields and/or the strain fields associated with macroscopic crystal deformations (e.g. bending, heat bump,...) and defects (e.g. distributions of impurities - growth sector boundaries and growth striations which are seen most frequently on the topographs of type Ib diamond samples). Figure 2.15 illustrates several types of defects [45].

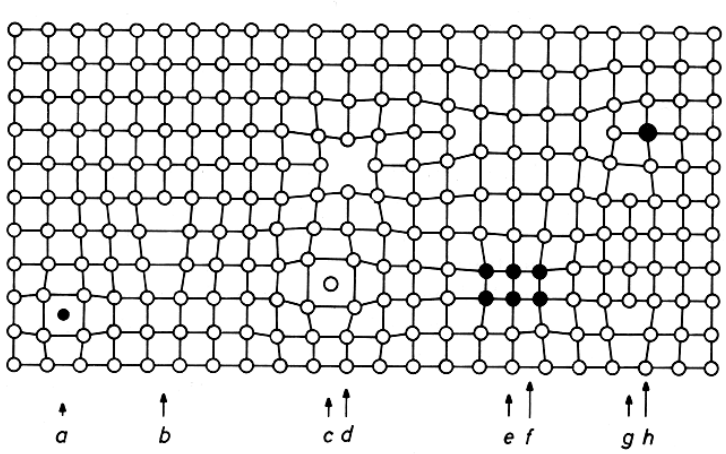

Figure 2.15: a) Interstitial impurity atom, (b) Edge dislocation, (c) Self interstitial atom, (d) Vacancy, (e) Precipitate of impurity atoms, (f) Vacancy type dislocation loop, (g) Interstitial type dislocation loop and (h) Substitutional impurity atom.

2.5.1 X-ray topography techniques

The classification of the different topographic methods depends on three basic elements, namely;

- the used source geometry and characteristics, including possible optical elements (slits, other crystals...),
- the sample properties and geometry, and
- the detector, also including possible optical elements

Only a limited selection of these techniques is of importance today from the practical point of view. There are two broad categories of the x-ray techniques, namely, the *extended beam techniques* and the *limited beam techniques*. Extended beam (wide area) is such that a beam diffracted by a perfect crystal plate (and a possible additional integration on the detector) shows homogeneous intensity, that is, no interference fringes are visible (figure 2.16). This will form the basis of this research and shall be discussed further in the next chapter.

Secondly, section topography (limited beam techniques) involves a restricted width (relative to the inter planar d-spacing) of the incoming beam perpendicular to the scattering plane, to a few micrometers (typically 10 – 20μm). Inhomogeneous intensity distribution is obtained after diffraction from a perfect crystal in the topograph. The rarely applied technique using an incoming beam restricted to several micrometers in two perpendicular directions is called *pinhole topography*. Limited beam techniques will not form part of this research. A scheme of the basic topographical techniques is given in figure 2.17.

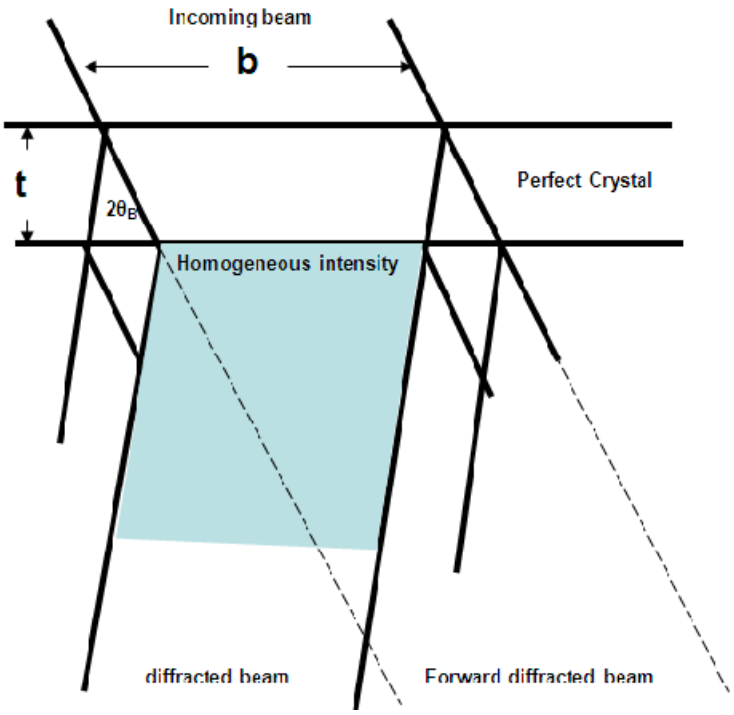

Figure 2.16: Schematic "definition" of an extended beam (example for the symmetrical Laue or transmission case).

2.5.2 Bragg and Laue geometries of x-ray topography

All topographic techniques techniques may be used in the *transmission* (or Laue) and the *reflection* (or Bragg) geometry. In the Bragg case (figure 2.18b), the incoming beam enters the sample and the diffracted beam leaves the sample through the same (entrance) surface. The forward-diffracted beam leaves the sample at the exit surface. In the Laue case (figure 2.18a), the incoming beam enters the sample through the entrance surface, and the diffracted as well as the forward-diffracted beams leaves the sample through the exit surface.

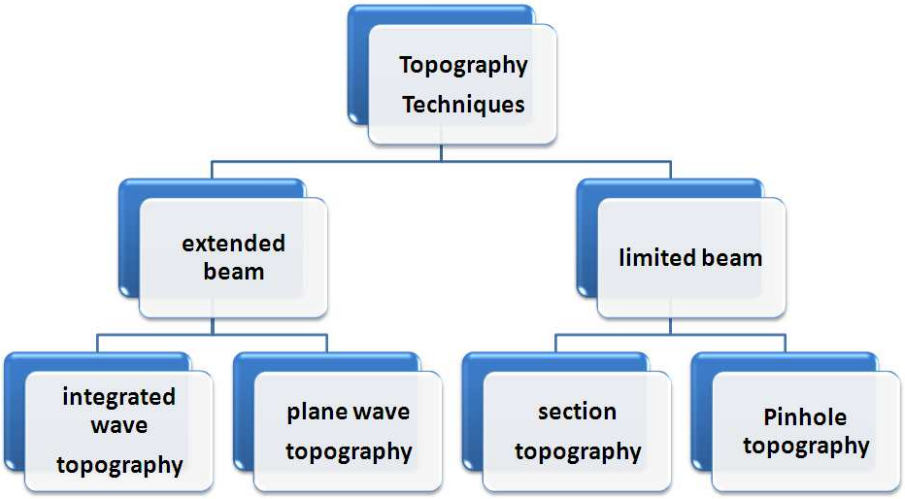

Figure 2.17: A scheme of the basic topographical techniques.

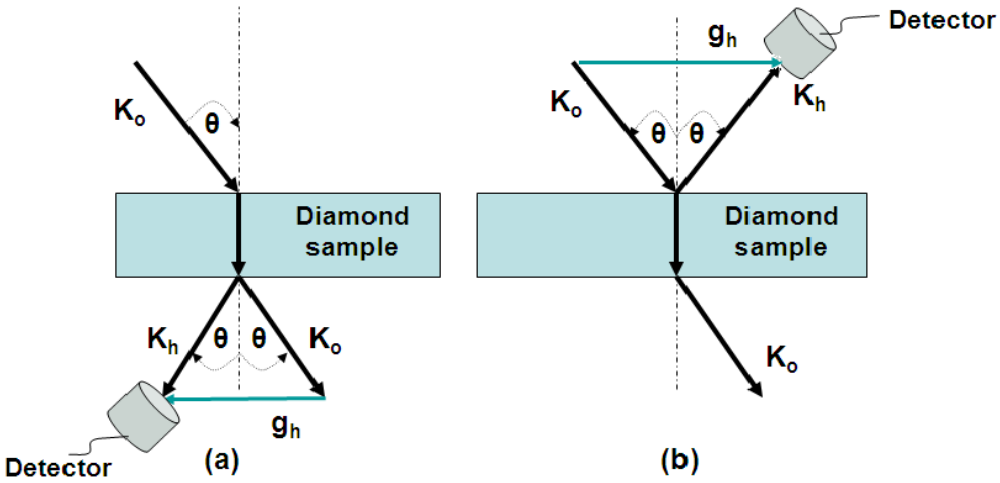

Figure 2.18: (a)Laue and (b)Bragg geometries of x-ray topography

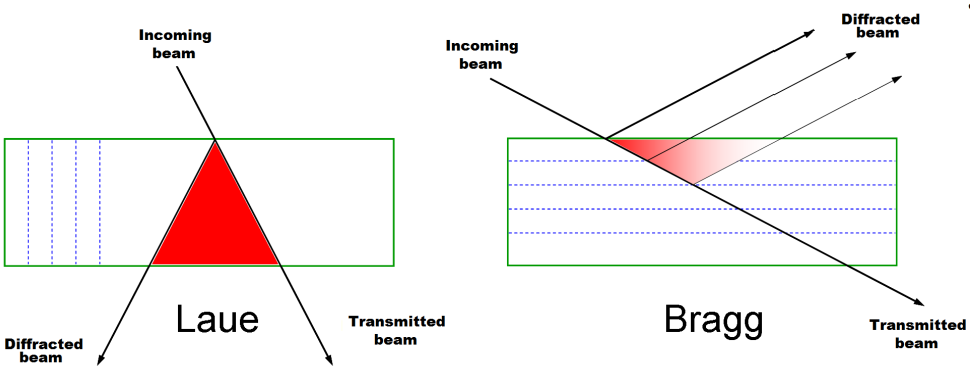

Figure 2.19: The different regions that are probed in Laue and Bragg geometry.

Either of the two geometries can be used to study both the near surface and bulk defects of the crystal. However, the reflection geometry is more sensitive to probe the near surface defects whereas the transmission geometry is mostly preferred for probing the volume of the crystal since in Laue case, the entire crystal volume is always visible.

2.5.3 Basic origins of contrast in x-ray diffraction topography

Defects inside a crystal may disturb the perfect lattice structure and produce long range strain fields. These distortion fields may affect the diffracted intensity and, so give contrast (non-homogenous intensity distribution) in the images produced, which are known as *topographs*. This process has the result that topography becomes a powerful tool for obtaining information about the departures from the perfect crystal structure. Origins of contrast in topography can be classified into structure factor contrast, orientation

contrast and the extinction contrast as briefly introduced below:

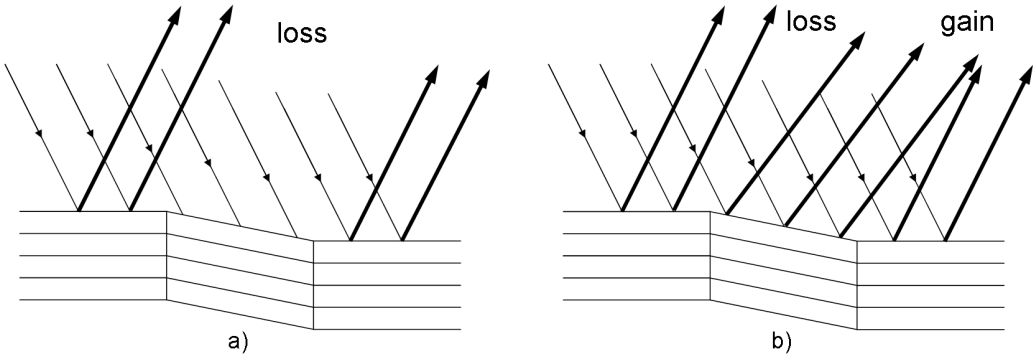

Figure 2.20: A schematic illustration of the formation of the orientation contrast. Note the local differences on the diffracted intensity and consequently to the image on the detector. In (a), the misorientation is larger than beam divergence and wavelength spread (e.g. parallel monochromatic beam) and in (b), the misorientation is smaller than beam divergence (e.g. polychromatic or divergent beam).

Structure factor contrast

Different materials or even different reflections of the same material have different structure factors. Similarly, different phases of the same material (e.g. for materials crystallizing in several different space groups) also have different structure factors. Structure factor contrast may appear in twinned crystals.

Orientation contrast

Orientation contrast arises from a crystal which contains lattice misorientations. For example, consider two perfect regions of the crystal which are misorientated with respect to one another. If a plane and monochromatic x-ray beam is used (or a beam with divergence smaller than the misorientation), the misoriented part will not diffract. This is illustrated in figure 2.20b, where the exiting angles of the respective diffracted beams will differ, leading to overlapping regions of enhanced intensity as well as shadows in the image, thus again giving rise to contrast [37]. The other region is outside the angular range of reflection and thus gives zero reflected intensity [46]. However, if a white x-ray beam is used, both regions may reflect but the two diffracted beams emerge at different angles (because the two regions select two different wavelengths); and separated images can be recorded on a relatively distant photographic plate.

Extinction contrast

Extinction contrast arises when the scattering power around the defects differs from that in the rest of the crystal. While structure factor and orientation contrasts result from simple considerations like Braggs law, the extinction contrasts can be understood based on dynamical theory as discussed in section 2.3.2. Interpretation of this contrast requires understanding of the dynamical diffraction effects occurring in thick, highly perfect crystals [37]. Topographic contrast of dislocations (as well as other defects) consists of direct, dynamic, and intermediary images (see figure 2.21 below), corresponding to the three different parts of an image from a defect showing extinction contrast. This kind of contrast may appear only when using techniques under integrated wave conditions (for example, white beam topography).

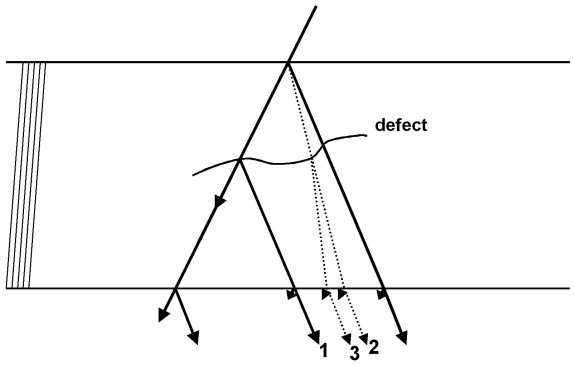

Figure 2.21: A schematic illustration of the formation of the diffraction contrast, formation of the three types of image around a defect: direct (1), dynamical (2) and intermediate image (3)

- the direct image, arise from the kinematical diffraction of x-rays that are not in Bragg condition for the perfect matrix (direct beam) by the strongly distorted parts of the dislocation (increase in intensity registered by the detector);
- the dynamical image, is formed from the loss of intensity (is a sort of screening made by the strongly distorted parts of the defects) of the wave fields propagating inside the crystal;
- the intermediate image, is due to the interference of the wave fields created by the defects and the wave fields propagating inside the perfect matrix.

Depending on the technique and the experimental parameters, but in particular on the absorption conditions, the relative contribution and contrast structure of the three image types may change considerably. Absorption conditions are defined by the product of the linear absorption coefficient μ and the effective thickness of the crystal t, traversed by the x-ray beam (i.e.

μt). For topographs recorded under low absorption conditions ($\mu t < 1$), the dislocation image is dominated by the direct image contribution, but the two others may be visible as well. The direct image appears as black double image (in the case of high spatial resolution), with slightly different gray levels. This difference may turn into black-white under intermediate absorption conditions, (about $5 > \mu > 1$). For high absorption cases (about $\mu t > 6$), only the dynamical contribution (known also as the Borrmann image) exists and the dislocation images appear on a film as white ones on darker background.

Defining the local dilation (i.e. relative change of the lattice parameter $\delta d/d$) and rotation (i.e. inclination angle of the reflecting lattice planes $\delta\varphi$ with respect to the perfect lattice) of the lattice, one parameter that basically controls the process in all variants of the dynamical diffraction theory for a deformed crystal is called the *effective misorientation* $\delta\theta(\vec{r})$. Effective misorientation may be obtained from equation 2.16, where θ_B is the Bragg angle.

$$\delta\theta(\vec{r}) = -\tan\theta_B \frac{\delta d}{d}(\vec{r}) \pm \delta\varphi(\vec{r}) \tag{2.16}$$

Chapter 3

Extended beam (wide area) characterization techniques

In this chapter, a brief introduction of the ID 19 beam line of the European Synchrotron Radiation Facility (ESRF) in Grenoble (France) will be presented. The chapter will also aim to address in detail the three main topographic techniques which were carried out at this beam line, namely; white beam topography (WBT), "monochromatic" beam topography (MBT) and the plane monochromatic wave topography (PMBT). The classification of the different topographic methods depends on three basic elements, namely; the used source geometry and characteristics, the sample properties and geometry and the detector. The main differences between these three techniques, such as their strain sensitivity to bulk and/or close-to-surface defects and the degree of difficulty to extract quantitative information will be highlighted.

Most diamond samples (mainly type IIa HPHT synthetic diamonds) discussed in this research were supplied by the Element Six (E6) diamond growers in South Africa.

ID 19 beam line

The ID19 beam line is installed on a low-beta section of the ESRF storage ring. There are primarily three insertion devices located in the straight section of this beam line. These are the two undulators and one wiggler. Any of these three insertion devices can be chosen as a source depending on the experimental requirements. ID19 is one of the longest (145 m) beam lines at the ESRF. It also has a small source size (30 μm vertical $\times$ 120 μm horizontal). The small source size and the long length of the beam line is an important characteristic of the beam line, especially for the geometrical resolution in x-ray imaging, good coherence properties (phase contrast imaging) and (not used at ID19 but at other beamlines) the possibility of extreme focusing. Equation 3.1 indicates how geometrical resolution ρ depends on the source size s, source to crystal distance Ł$_o$ and crystal to film or detector distance D as depicted from figure 3.1. The smaller the value of the angular source size $\delta = s/L_o$, the higher the geometrical resolution ρ will be, where

$$\rho = sD/L_o = \delta D \tag{3.1}$$

It is possible to distinguish between orientation and extinction contrast by recording topographs very close (extinction contrast is pronounced) and very far from the sample (orientation contrast is pronounced) using the ID 19 beam line.

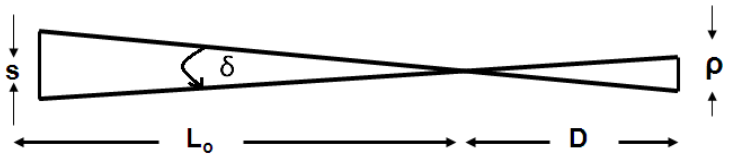

Figure 3.1: A schematic diagram showing the geometrical resolution limit set by the projected source height normal to the incident plane.

3.1 Integrated wave topography

A process in which a *divergent* and/or *non-monochromatic* incoming x-ray beam is used to record a topograph is called *"integrated wave topography"*. As such, the integrated wave topography technique does not employ a single plane-wave, a monochromatic wave or a cylindrical-monochromatic wave, but a superposition of such waves. For this integration to take place, the angular source size δ has to be greater than the full width at half maximum of a reflectivity curve (i.e. $\delta > w_h^\theta$) and/or the spectral width of the incoming beam must be greater than the full width at half maximum of a reflectivity curve (i.e. $\Delta\lambda_s > w_h^\lambda$). The white beam mode satisfies this condition since $\Delta\lambda_s >> w_h^\lambda$ and since the beam is always non-monochromatic. Other examples of integrated wave topography are Lang (projection) topography as well as the Berg Barrett topography [47, 48, 49].

"Monochromatic" beam topography

Two or more crystals are usually used in topographic set-ups to enhance strain sensitivity and to suppress the background from the radiation which is not used in the image formation. There are basically two important settings

of the possible two- or more crystal systems, namely the non-dispersive (fig. 3.2) and the dispersive settings.

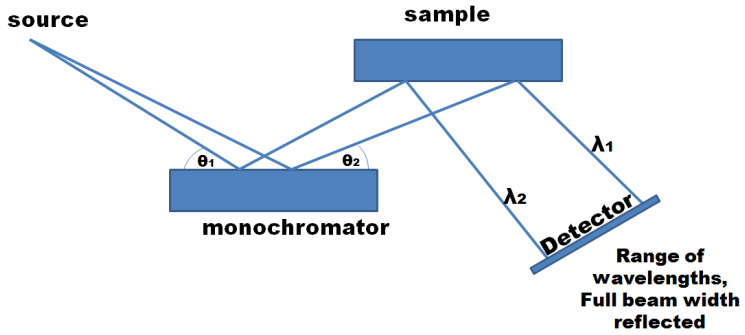

Figure 3.2: Non-dispersive setting (+n,-n) setting. The two crystals are identical and the same reflection is used on both. The diffraction vectors are anti-parallel.

In the non-dispersive set-up, the two crystals used have to be identical and the same reflections must be used on both the sample and the beam conditioner. Different crystals and/or different reflections may be used in dispersive set-ups. The "monochromatic" beam topography can be used in both the integrated wave technique (with a much narrower energy band or spectrum) as well as the plane and monochromatic wave configuration technique (with $d << w_h$). The latter (to be discussed further in section 4.3) is a special variant of the double crystal set-up that the team have used in this research to obtain strain sensitivity in the low 10^{-8} regime. To achieve this, a double crystal set-up was used with a monochromatic incident beam integrating over a range bigger than, but comparable to, the reflectivity curve of the crystal in the energy space. This was achieved by using a silicon beam conditioner to control the divergence and wavelength spread of the beam.

A combination of diffracting elements and angular limiting apertures were used. This way, the spectral width of the beam could also be controlled. The beam from the beam conditioner was then allowed to fall upon the specimen (diamond sample) whose orientation could also be adjusted. While using the technique, the diffracted beam left the sample and entered the detector or film which accepted all the beams scattered off the diamond sample.

3.2 Plane and monochromatic wave topography

Plane-wave topography is special variant of double crystal topographic technique, which is mainly used to enhance strain sensitivity. There are only few methods known that are able to measure strain inhomogeneities in nearly perfect crystals with strain sensitivity in the low 10^{-8} regime. In this research, the double crystal (+n,-m) setup has been used in the non-dispersive mode, where "n" and "m" indicates that different crystals (i.e. silicon monochromator and the diamond sample) were used and that different reflections may also be used on both. The "+" and "-" signs indicates the opposite manner in which they reflect the x-ray beam (see figure 3.2). The non-dispersive mode was achieved through the local adaptation of Bragg angles, to compensate either dispersion or a bending of the sample using a bendable highly perfect silicon monochromator in a versatile instrument allowing the investigation of all kinds of crystals with high strain sensitivity and without any reduction in image size. This way, the incident beam on the diamond sample was approximately a plane x-ray wave in a localized region of space.

The double crystal rocking curves had a section on each flank that is linear to a good approximation, and at the same time being the steepest part of the curve. In cases were the local deformation was so small that the related effective misorientation shifted the working point on the rocking curve only within that linear part, then there was also a linear dependence of the local reflected intensity on the effective misorientation. This relationship was used to quantify the deformations in the crystal. Films were digitised using an optical microscope LEICA MZ16 connected to a CCD camera LEICA DC300.

In order to further increase the strain sensitivity of the plane-wave topography technique, successive high-order reflections and correspondingly higher energy x-rays were used. In this way the double crystal rocking curves (the autocorrelation function of sample and monochromator reflectivity curves) with extremely steep flanks were obtained. The topographs obtained using this technique showed much more details (strain sensitivity) compared to the white beam topographs. The contrasts were also relatively "simple" to calculate (as shall be performed later in chapter 4).

Experimental conditions for the plane and monochromatic wave topography

The plane and monochromatic wave topography technique offered a very difficult setup technique compared to the other topographic techniques. In order to achieve diffraction conditions, the sample under study must be precisely aligned because the contrast observed strongly depends on the exact position of the angular working point on the rocking curve of the sample (i.e. on the angular distance between the actual sample rotation position and the theoretical position of the Bragg peak). A sample rotation stage stepping in

the hundredth of an arc-second range is therefore an essential instrumental precondition for controlling and varying the contrast conditions [15].

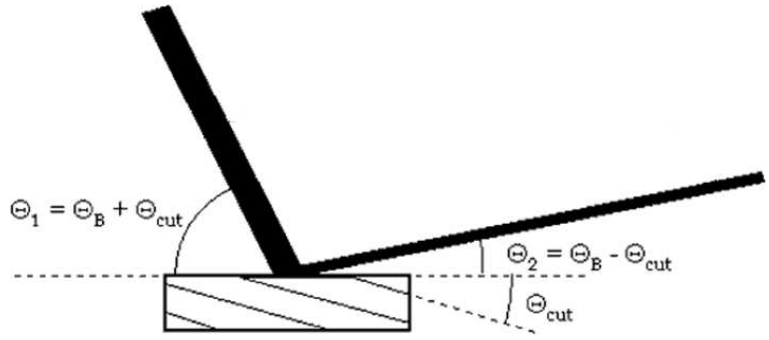

Figure 3.3: Parameters for an asymmetric reflection with Bragg angle θ_B on the diamond sample. All crystal surfaces were along the $< 001 >$ direction. θ_{cut} is the angle between the scattering crystal-planes and the $< 001 >$ surface.

In order to locate the desired reflections from the diamond sample and to cast it on a photographic film or detector, the asymmetry angle must be taken into consideration. The surfaces of both the silicon monochromator crystal and the diamond sample were cut along the [001] plane. The sample and monochromator crystal alignments has been illustrated in figure 3.3

Sample	Bragg/Laue	Silicon hk1	Diamond [hkl]	Energy keV	Film No.	Silicon θ_B	diamond θ_B	Asymmetry Angle θ_{cut}
1	B	[4 4 4]	[$\bar{1}$15]	12	06101402	41.2	48.8	15.79
3	B	[4 4 4]	[$\bar{1}$15]	12	06101501	29.6	48.8	15.79
3	B	[4 4 4]	[$\bar{1}$15]	12	06101502	29.6	48.8	15.79
3	B	[4 4 4]	[115]	16	06101504	29.62	21.8	15.79
1	B	[8 0 0]	[800]	20	06101601	27.2	44.02	0.00
2	B	[8 0 0]	[800]	20	06101602	27.2	44.02	0.00

Table 3.1: A summary of the experimental setup for the plane and monochromatic wave topography

Chapter 4

Results and discussion

Results of the synchrotron based x-ray topography will be discussed in this chapter. The chapter will start by first addressing itself to the qualitative techniques (i.e. integrated wave techniques) followed by the quantitative plane and monochromatic wave topography technique.

4.1 Local rocking curve broadening in type IIa HPHT diamond specimens

Figure 4.1 shows the statistical distribution of rocking curve width broadening for three types of HPHT synthetic diamond material, namely, type IIa HPHT diamond by Burns et.al [8], type IIa from an earlier batch of material and type Ib measured at ESRF by Hoszowska et.al [15]. The points correspond to the frequency with which different values of the rocking curve width broadening occur for different points on the crystal, over the whole crystal. In some cases the data of several crystals are averaged. These results have been presented in table 4.1 below. The current material show negligible broadening in the central cubic growth sector region implying that the method is not sensitive enough to depict defects at this level of quality in the diamond samples, which necessitates x-ray topographical methods with high strain sensitivity and local resolution to be used.

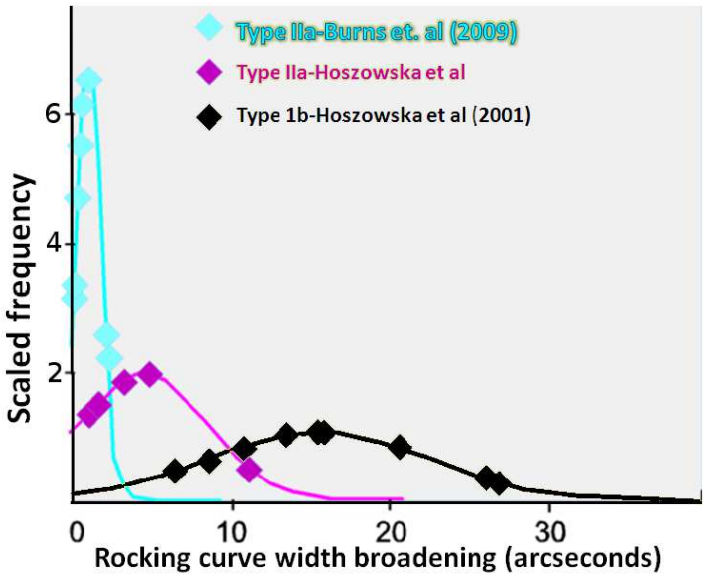

Figure 4.1: Statistical distribution of rocking curve width broadening for three types of HPHT synthetic diamond material.

Sample	Theoretical width	Exp. width full beam	Broadening full beam	Exp. width 100μm center	Broadening center
1173-001a	1.045″	1.15″	0.48″	1.10″	0.20″
1173-001b	0.986″	1.39″	0.98″	1.03″	0.20″
1173-001d	1.056″	1.30″	0.76″	0.97″	0.0″
1173-001e	1.018″	2.36″	2.13″	1.03″	0.30″
1186-001a	1.021″	1.09″	0.38″	1.04″	0.20″
1186-001c	1.021″	1.14″	0.52″	1.09″	0.38″
1186-001d	1.021″	2.47″	2.25″	1.73″	1.40″
1149/13R	1.059″	1.33″	0.80″	1.13″	0.39″

Table 4.1: Rocking curve broadening results for type IIa HPHT diamonds specimens. The theoretical widths were calculated using the XOP software package.

4.2 Integrated wave topography

Typical defects observable through the white beam topography

Figure 4.2 below is an x-ray white beam topograph [$\bar{2}20$] reflection of a type IIa diamond plate. This serves a typical example of which exhibits features related to various defects. Identifiable defects on figure 4.2 will be discussed individually in this section

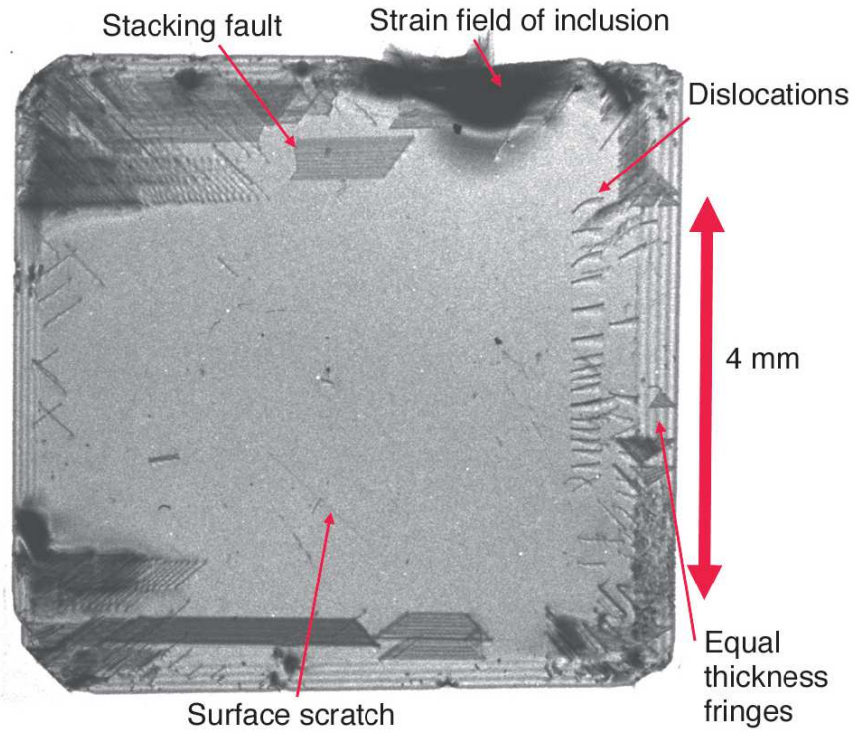

Figure 4.2: X-ray white beam topograph [$\bar{2}20$] reflection of a type IIa diamond plate.

Stacking faults

A stacking fault is a one- or two-layer interruption in the stacking sequence of layers of atoms in a crystal. Stacking faults may occur in a number of crystal structures especially in close-packed structures. For example, face-centered cubic (fcc) and hexagonal close-packed (hcp) structures both have close packed atomic planes with sixfold symmetry (the atoms form equilateral triangles) and differ only in their stacking order. When stacking one of these layers on top of another, the atoms are not directly on top of one another. This has been illustrated in figure 4.3, in which the first two layers are identical for hcp and fcc, and labeled AB [45]. If the third layer is placed so that its atoms are directly above those of the first layer, the stacking will be ABA – this is the hcp structure, and it continues ABABABAB. Several stacking faults can be identified on figure 4.2, one being around the middle top part next to the large strain field due to inclusions.

(a) 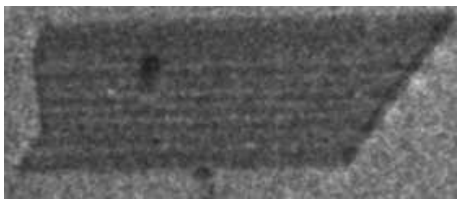 (b) 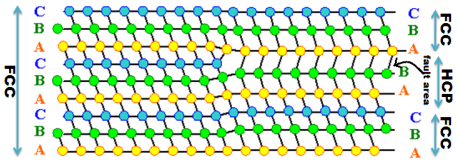

Figure 4.3: (a) A zoomed image of one of the stacking faults in figure 4.2 along the indicated undistorted reciprocal lattice vector h and (b) a schematic side view of a dislocation

.

However, there is another location for the third layer, such that its atoms are not above the first layer. Instead, the fourth layer is placed so that its

atoms are directly above the first layer. This produces the stacking ABCAB-CABC, and is actually a cubic arrangement of the atoms. Stacking faults may be identified as gray fringe patterns. Stacking faults in diamond tend to lie on [111] but, for a given [220] diamond reflection, stacking faults will only be observed for two of the [111] planes because for the other two the fault vector lies in the diffraction plane [50]. The fault vectors f of stacking faults may also be determined by x-ray topography, using the criterion for invisibility $g.f = m$, where m is an integer. In diamonds, f is either $\frac{1}{3}[111]$ for an intrinsic type of stacking fault or $\frac{2}{3}[111]$ for the theoretically possible extrinsic stacking fault [51]. Stacking faults have been established in almost all crystals, and they are always situated in [1 1 1] planes, occasionally crossing the whole crystal. In the crystals grown in $< 111 >$ direction stacking faults are typically localized in the regions containing dislocations.

Metal inclusions

There is a large strain field visible on the top part of figure 4.4 due to the inclusion inside the material. Inclusions are, under the used absorption conditions, always identified by a dark (black) contrast in topographs. The inclusion takes at room temperature a different volume than during its incorporation and so it is pressing or pulling on the surroundings, creating compressive or tensile strain and changes the average local lattice parameter. An estimation of the maximum distortion due to the inclusion has been made using the geometrical sketch in bottom of figure 4.4 [4].

The distance between the core of the inclusion (measured from the middle of the strain field) and the outermost deformed part of the image, d, has been used in a simple geometrical calculation together with the sample to film

distance L and the distance from the beam-stop shadow to the topograph P to calculate the misorientation angle $\delta\theta$ as illustrated below:

$$\delta\theta = \sin^{-1}\left(\frac{d}{L\prime}\right) = \sin^{-1}\left(\frac{d}{\sqrt{L^2+P^2}}\right) = \sin^{-1}\left(\frac{0.9}{\sqrt{23^2+8.2^2}}\right) = 3{\times}10^{-3}rad \tag{4.1}$$

Growth sector boundaries and growth striations

The presence of different nitrogen concentrations in different growth sectors results in different average lattice parameters in these different growth sectors. Therefore, lattice planes between two regions with different N-concentration are distorted at their boundaries. This leads to strain fields between growth sectors as illustrated schematically in figure 4.5. Local impurity concentration fluctuations within a growth sector are called growth striations. The dilation of the diamond lattice has been found to depend upon the P_1 nitrogen impurity content according to the Lang's dilatation formula (equation 2.2)[8].

The lattice parameter of diamond increases with increasing nitrogen content because of the relaxation of the inter-atomic bonds caused by the additional electron which is introduced by each nitrogen atom. Nitrogen has one electron more than carbon being $2s^2\ 2p^3$ where carbon is $2s^2\ 2p^2$. The additional electron occupies an anti-bonding $2s^3$ orbital.

Figure 4.6 shows a Ib diamond sample topograph with different growth striations [4]. These are clearly visible in the figure as parallel lines normal to the growth direction and parallel to the growth surfaces. Their origins are small fluctuations of growth parameters within the growth sector during the synthesis.

(a)

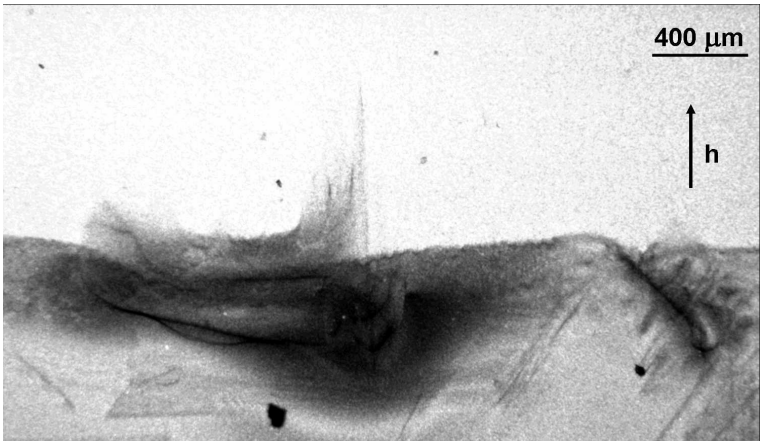

(b)

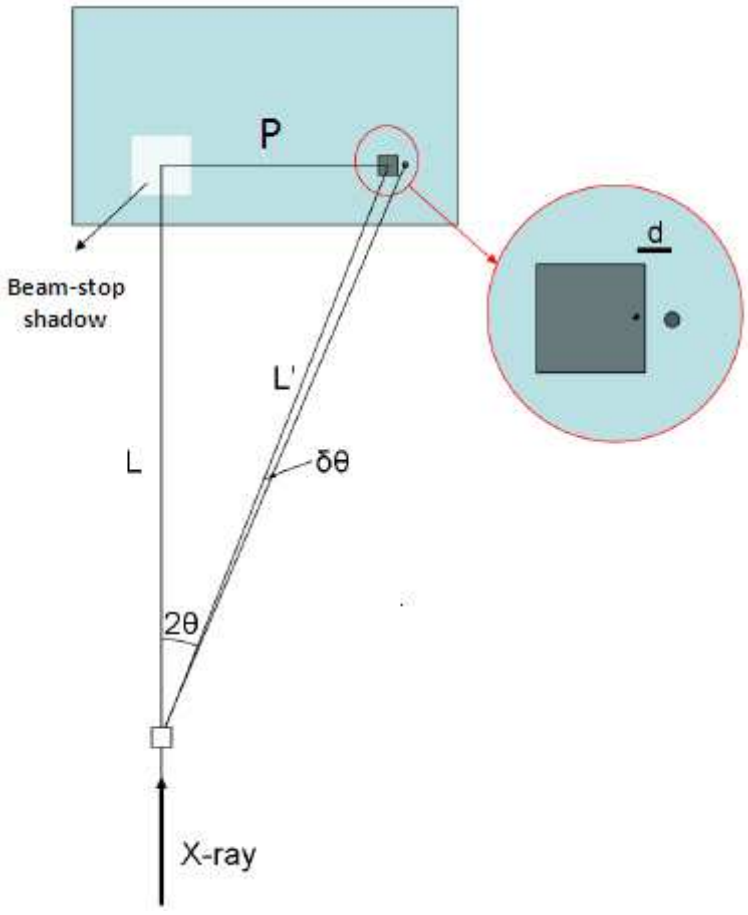

Figure 4.4: (a) A zoomed image of the inclusion in figure 4.2, where $\vec{h}$ is the undistorted reciprocal lattice vector and (b) is a geometrical method of estimating distortions due to an inclusion.

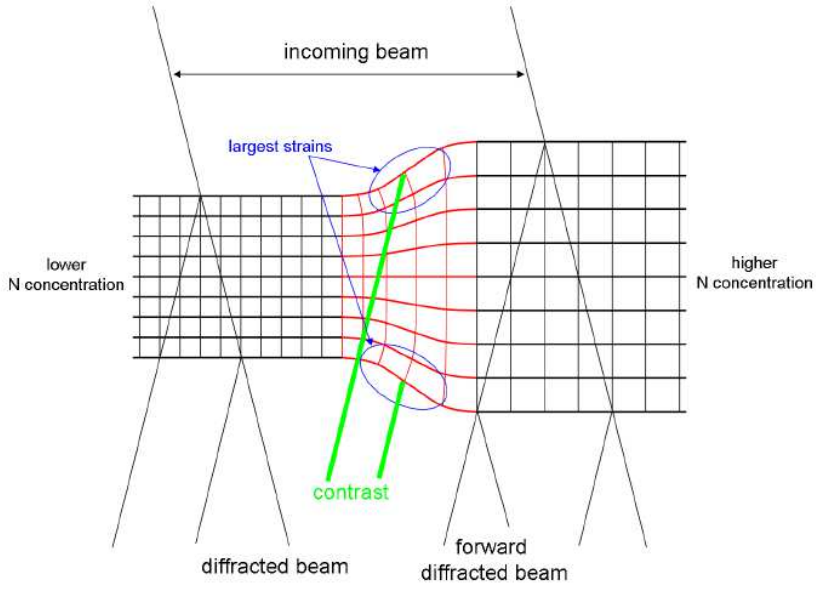

Figure 4.5: A perspective view of growth sector boundaries between two different growth sectors with different nitrogen(N) concentrations.

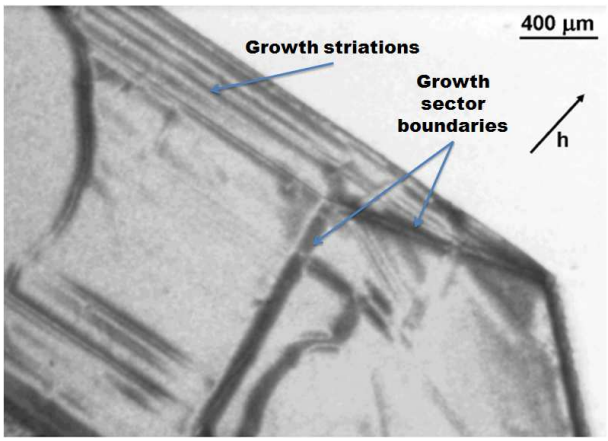

Figure 4.6: Different growth sectors in a Ib type diamond (white beam, Laue geometry [040] reflection), where $\vec{h}$ is the undistorted reciprocal lattice vector.

.

Equal thickness fringes

Pendellösung or equal thickness fringes in topography occur due to a kind of "bounce" in energy between the forward diffracted and the diffracted beams. According to Kato and Lang [7], pendellösung fringes occur when two wave fields, each associated with a point lying on a different branch of the dispersion surface (a three-dimensional plot of the frequency versus planar wave vectors) interfere. It is also possible to observe these fringes due to the variation of their periods $\wedge_o$ with wavelength. Several pendellösung fringes can be identified on figure 4.2 (e.g. on the right, left, and bottom parts). Figure 4.7 schematically illustrates the creation of pendellösung fringes in a wedge-shaped crystal.

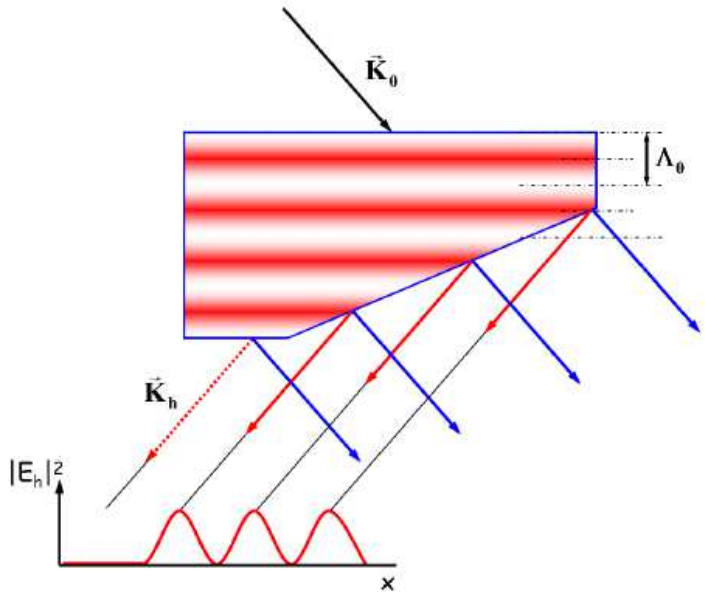

Figure 4.7: Schematic illustration of the formation of equal thickness fringes in a wedge-shaped crystal

The thickness of the crystal was estimated by multiplying pendellösung distance Λ_o (see equation 2.12) by the number of fringes counted from the topograph. The pendellösung distance is amongst others depending on the structure factor and has been calculated for the experimental conditions of this topograph using the XOP software package as 96 μm using an energy of 34 keV and a total of 4.75 fringes as counted from the image (i.e. the actual number of fringes could not be ascertained since the fifth fringe was suspected in the left part of the image, where the contrast is weaker). This gives a thickness of between 456 to 480 μm, which is in perfect agreement with the value provided by the manufacturer, 480 μm.

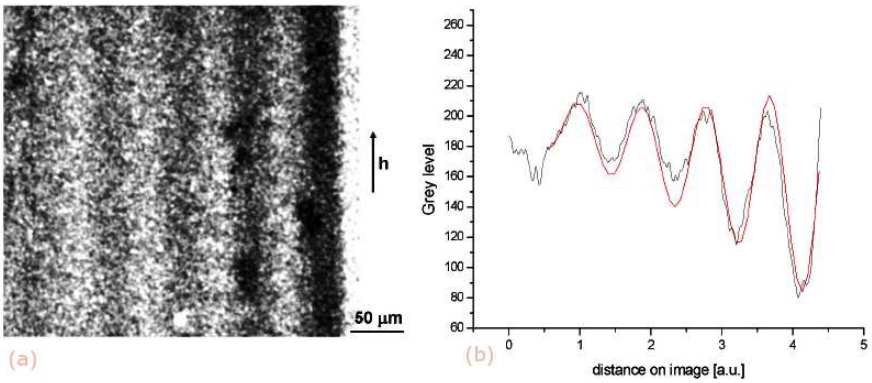

Figure 4.8: (a) A zoom of the equal thickness fringes showed from the top right corner of figure 4.2 and (b) a profile plot of the different intensities on the image using the XOP program (right)

An image processing program known as ImageJ obtainable from [52] was used to obtain a profile plot (black curve) in figure 4.8(b) of the zoomed image of the fringes in figure 4.8(a) which was then fitted using several Gaussians using the Origin spreadsheet[4].

Dislocations

Dislocations are linear defects which are mainly comprised of two basic types, namely; edge dislocation and the screw dislocation. A combination of an edge dislocation and a screw dislocation is called a mixed dislocation [49]. These dislocation types can be identified by the orientation of a unit vector in the direction of the dislocation line $\bar{l}$ relative to the magnitude and direction of the distortion Burgers vector $\bar{b}$ as indicated below; .

- For a perfect screw dislocation, $\bar{b} \parallel \bar{l}$ and therefore $\bar{b} \times \bar{l} = 0$
- For a pure edge dislocation, $\bar{b} \perp \bar{l}$ and so $\bar{b}.\bar{l} = 0$
- For a mixed dislocation, $\bar{b}$ is at an angle to $\bar{l}$ that is greater than 0° but less than 90° (i.e. $\bar{b} \times \bar{l} \neq 0$ and $\bar{b}.\bar{l} \neq 0$).

For the present case of low absorption ($\mu << 1$), thick crystal (with $A = \pi t/\Lambda_0$ "thick" means $A >> 1$), extended beam and integrated wave topography, these dislocations may be identified as black (high intensity) lines, or double lines (the so-called direct images of dislocations). For thinner (thinner than the Pendellösung length) crystals, no direct images of dislocations are observable.

Figure 4.9 shows perspective view of a screw and edge dislocations with the dislocation line $\bar{l}$ and the dislocation Burgers vector $\bar{b}$ clearly illustrated [45]. In figure 4.10, the distance between direct (black line) and dynamical (brighter shadow) images is bigger on the right hand side of the dislocation image, implying that the dislocation is closer to the entrance surface of the x-ray (i.e. towards the source). On the left hand side, the two images are closer together indicating that the dislocation is close to the exit surface (i.e.

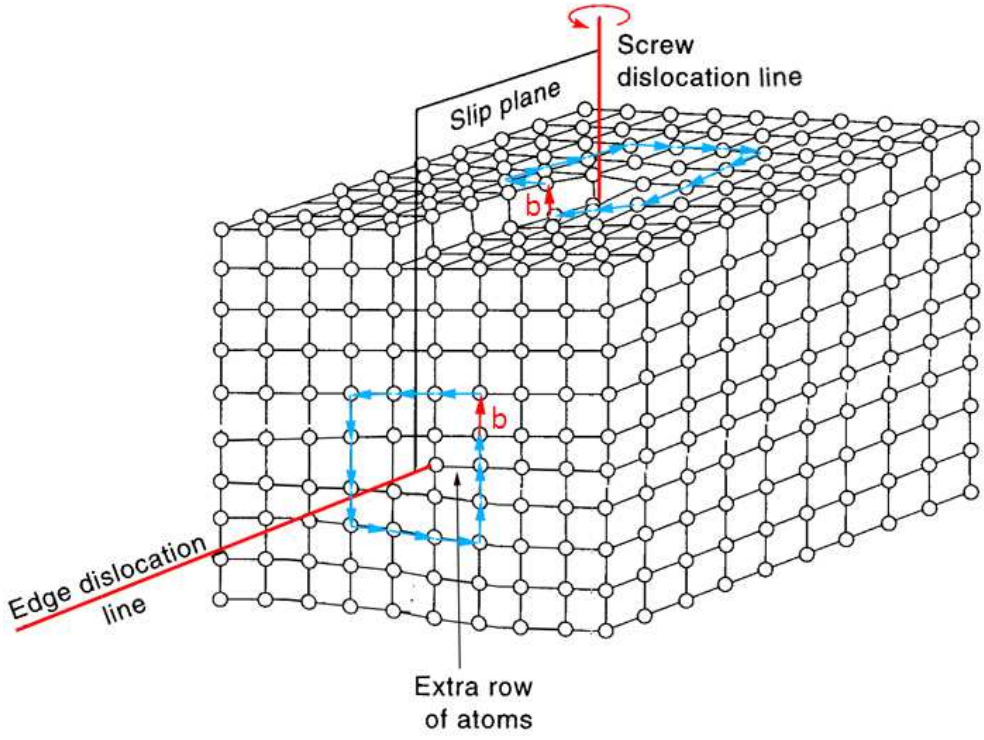

Figure 4.9: A perspective view of a screw and edge dislocations. The dislocation line $\bar{l}$ and the dislocation Burgers vector $\bar{b}$ have been indicated in each case.

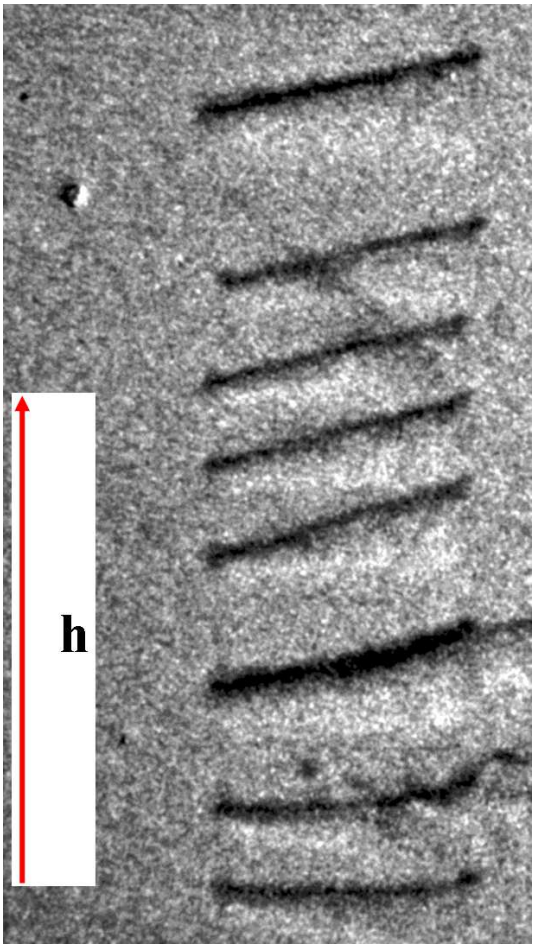

Figure 4.10: A zoomed portion of the dislocation image from figure 4.2 right hand side. The black line is the direct image and the brighter shadow is the dynamical image.

towards the detector) [53]. One also notices that the dislocations in figure 4.10 are threading dislocations, passing through the crystal plate, intersecting the entrance and the exit surface.

For crystal deformations by the displacement u from the perfect lattice state, the electron density becomes

$$\rho(\acute{r}) = \rho(r+u) = (1/V)\Sigma F_g \exp[-2\pi i g.(r+u)] \tag{4.2}$$

where r is a lattice vector, V is the volume of the unit cell, F_g is the structure amplitude for reflection g and $\exp[-2\pi i g.u]$ is the extra phase factor. The displacement vector around a mixed dislocation is given by

$$u = Pb + Q(b \times l) + R(l \times b \times l) \tag{4.3}$$

The exact forms of expressions P, Q and R are unimportant in the present discussion but they are given here for completeness. They contain the Poisson's ratio σ and they are written in cylindrical polar coordinates (r, θ, z), with z measured along the direction l of the dislocation line and θ measured from the plane containing b and l [54].
$P = \frac{\theta}{2\pi}$,
$Q = \frac{1}{2\pi}\Big[\Big(\frac{1-2\sigma}{2(1-\sigma)}\Big)\ln r + \frac{\cos 2\theta}{4(1-a)}\Big]$,
$R = \Big[\frac{\sin 2\theta}{8\pi(1-\sigma)}\Big]$

The strain field around a perfect screw dislocation ($b \parallel l$ or $b \times l = 0$) is given by $u = Pb = \frac{\theta}{2\pi}b$ and therefore invisible when $g.b = 0$. The strain field around a pure edge dislocation ($b \perp l$ or $b.l = 0$) is given by $u = (P+R)b + Q(b \times l)$ and therefore invisible when $g.b = 0$ and when $g.(b \times l) = 0$ (i.e $g \parallel l$). A mixed dislocation is never completely invisible since g cannot simultaneously

satisfy $g.b = 0$, $g.(b \times l) = 0$ and $g.(l \times b \times l) = 0$ [45].

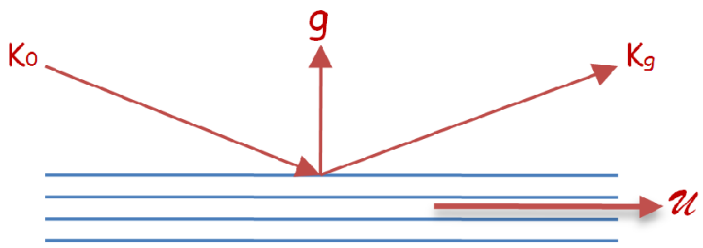

Figure 4.11: A schematic illustration of the atomic displacement parallel to the Bragg planes and perpendicular to the diffraction vector g. The Bragg reflection will not be influenced by displacement of atoms perpendicular to the diffraction vector.

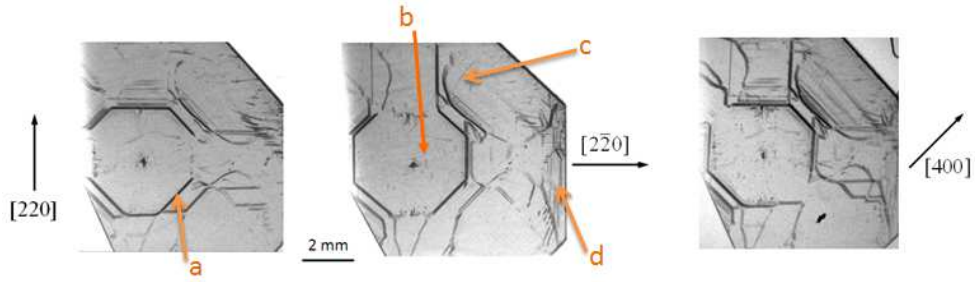

Figure 4.12: Three white beam topographs of a type Ib diamond plate with [100] orientation taken in transmission geometry, with a) Growth sector boundaries, b) dislocations, c) surface scratch and d) growth striations. The arrows indicate the diffraction vector along the direction of the undistorted reciprocal lattice vector h.

.

A schematic illustration of the atomic displacement parallel to the Bragg planes and perpendicular to the diffraction vector g is illustrated in figure

4.11. The Bragg reflection will not be influenced by displacement of atoms perpendicular to the diffraction vector (i.e. $g \perp u$ or $g.u = 0$) [45]. Figure 4.12 shows a $\langle 100 \rangle$-oriented type Ib HPHT diamond [220], [$2\bar{2}0$] and [400] reflections. All topographs were taken from one film. From the extinction rule $u.g_h = 0$ we conclude that no displacement field components of growth sector boundaries perpendicular to the diffraction vector do exist (i.e. the growth sector boundary labeled a. above has only components in planes perpendicular to the direction of the 400 diffraction vector).

With reference to figure 4.11 and 4.12, the effective misorientation equation previously defined in equation 2.16 may be written in the following form

$$\delta\theta(\vec{r}) = -\frac{\lambda}{2sin\theta_B}\frac{\partial[\vec{h}.\vec{u}(\vec{r})]}{\partial s_h} \tag{4.4}$$

to explain the difference in features observed in the three topographs, where $\vec{h}$ is the undistorted reciprocal lattice vector, $\vec{u}(\vec{r})$ is the displacement vector field and $\partial/\partial s_h$ is the differentiation along reflected beam direction.

White beam topographs of three diamond samples

Figure 4.13 below shows white beam topographs of the three HPHT synthetic type IIa diamond samples studied in this research. The [040], [220] and [$\bar{2}$20] reflections are labeled (a), (b) and (c) respectively. All three reflections were recorded on the same film due to a wide range of available wavelengths.

Sample 1 has a metal inclusion close to its center visible on all three reflections. There are also stacking faults visible on the top part the sample mainly visible on the [040] and [$\bar{2}$20] reflections but not visible on the [220] reflection implying that the burgers vector of the dislocations bordering the stacking faults are perpendicular to the [220] but not to the [$\bar{2}$20]. Several other defects are visible along the edges away from the central cubic growth sector region.

Sample 2 has been extensively discussed in section 4.2. One easily identifiable defect on this sample is the metal inclusion on the top part of all three reflections. The white beam topography reveled excellent bulk properties for this sample especially its central cubic growth sector region which is relatively free from identifiable defects such as stacking faults and dislocations.

Sample 3 is a wedge-edged crystal with several surface scratches visible on the top right hand corner. All three samples have central regions generally free of defects detectable through the white beam topography. These samples will later be analyzed through a more sensitive plane and monochromatic wave technique to illuminate the strain fields in the cubic growth sector regions.

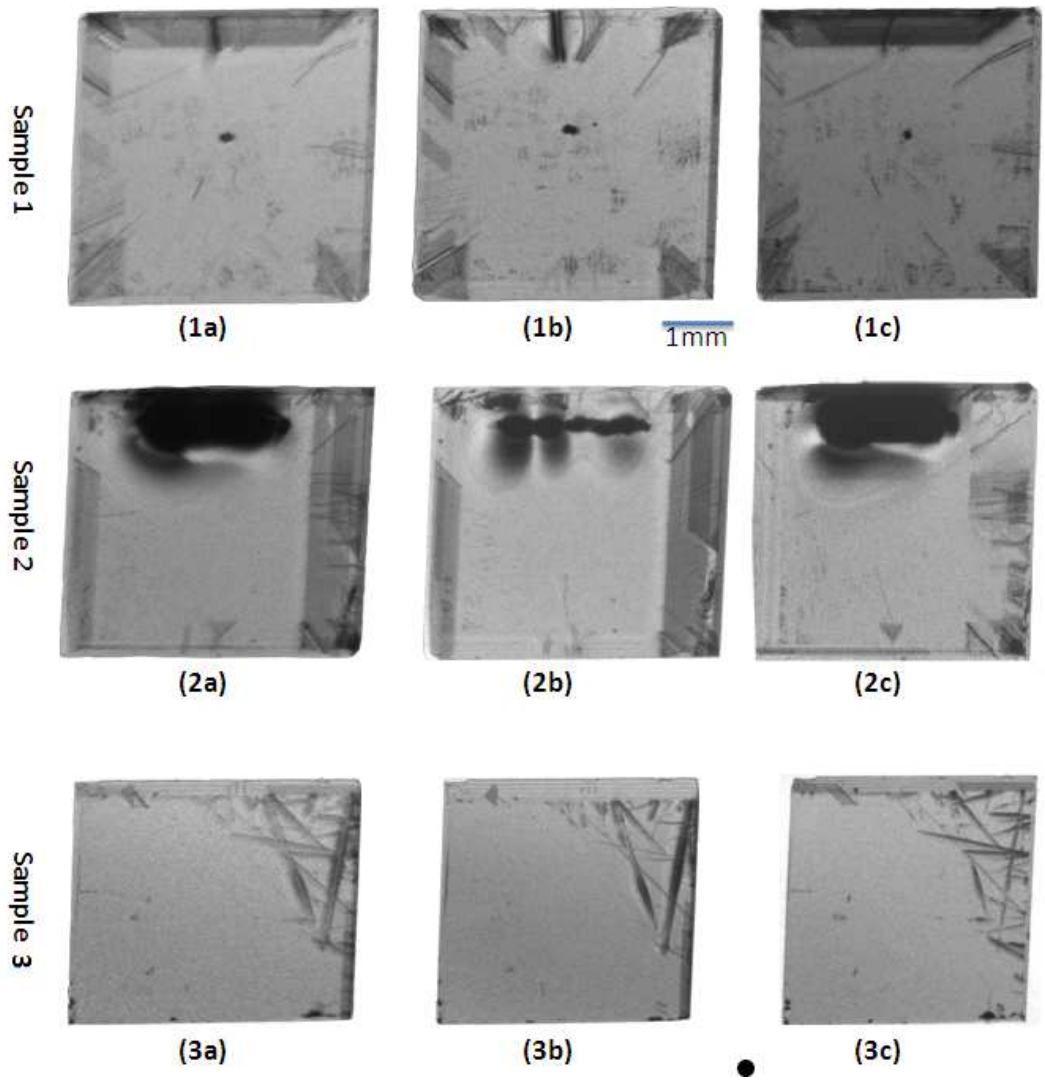

Figure 4.13: White beam topographs of sample 1-3 (HPHT synthetic type IIa diamond samples). The labels (a), (b) and (c) are the [040], [220] and [$\bar{2}$20] reflections respectively. All three samples have central cubic regions generally free of defects detectable through the white beam topography. These samples will later be analyzed through a more sensitive plane and monochromatic wave technique to illuminate the strain fields in the cubic growth sector region

.

"Monochromatic" beam topography

The monochromatic beam topography experiments were performed at the ID19 beam line of the ESRF. The technique yields relatively more detailed results (sensitivity) compared to the white beam topography due to its higher strain sensitivity. The increased strain sensitivity of the monochromatic beam technique relative to the white beam technique is demonstrated in figure 4.14 where the surface was left partly incompletely processed. The lower left part was not fine-polished to completion, showing several scratches. The rest is nearly defect-free, showing mainly three isolated single dislocations labeled A, B and C. Note that at this low level of strain, the surface imperfections (scratches not visible under optical examination) contribute significantly to the extended strain fields in the sample. A few extended strain fields from the three isolated single dislocations are also visible.

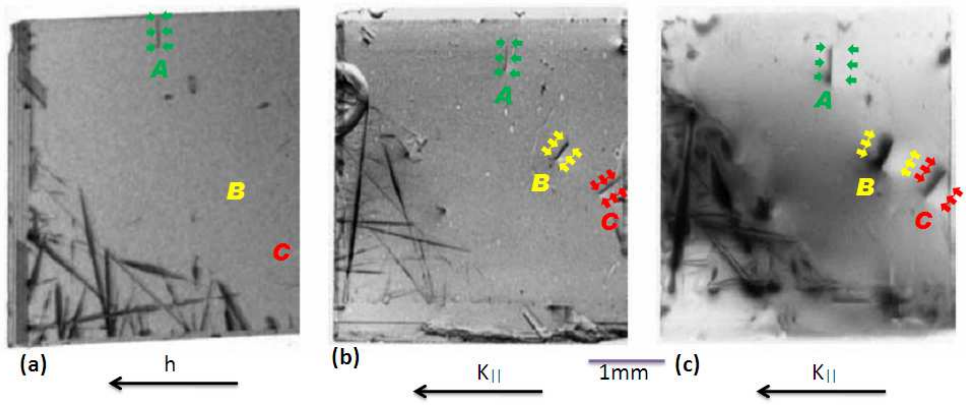

Figure 4.14: A comparison of the three topographs . Figure (a)⟶ (c) left to right, comparing (a) white beam topograph, (b) and (c) are two double crystal topographs of the same sample taken with different strain sensitivities.

In figure 4.14(a), this sample is viewed in white beam conditions, and in figures 4.14(b) and 4.14(c), in double crystal topography conditions at two different strain sensitivity settings. Figure 4.14(a) is in Laue geometry and 4.14(b) and (c) are in Bragg reflection geometry. For figure 4.14(b), the settings were E_γ=12 keV, with the [444]-reflection of the silicon monochromator (Darwin width 1.00″) and the 115-reflection of the diamond sample (Darwin width 1.02″). The theoretical detection limit is about 4×10^{-8}. The settings for figure 4.14(c) were E_γ=20 keV using [800]-higher order reflections on both the silicon monochromator (Darwin width 0.31″) and the diamond sample (Darwin width 0.25″). In this case, the theoretical detection limit is about 1.2×10^{-8}. Therefore, one notes clearly the increase in the strain sensitivity as higher order reflections and higher energies are used. This is clearly evident from figure 4.14(c), as opposed to the previous two topographs which shows clearly the strain field around the defects [55]. This will be explained further in a subsequent section. One should be able to follow the increase of the width of the same object (i.e. dislocation A,B or C) from (a)$\longrightarrow$ (c) topographs. The resulting macroscopic extensions is almost doubled as we observe from topograph (a)$\longrightarrow$(c)) [55].

4.3 Plane and monochromatic wave topography

In this section, results of the plane and monochromatic wave topography technique shall now be presented. The double crystal rocking curves were recorded while rotating the diamond sample crystal through an angle θ relative to the silicon monochromator crystal. These double crystal rocking curves, presented in figure 4.19–4.22 were very narrow (few arc seconds) and had a section on their flanks that was linear to a good approximation, at the same time being the steepest part of each curve. Although topographs were taken at several working points along each double crystal rocking curve, only the one taken at the steepest part of the flank was used through the quantification procedure. At the steepest linear flank of the rocking curve, a small variation of the local Bragg angle $\delta\theta$ yields a proportionately large variation of the reflectivity δR. This has been illustrated in figure 4.15. If $\delta\theta << w_h^\theta$ and the angular position of the working point θ_A is on the linear part of the rocking curve, the double crystal reflectivity δR is directly proportional to the effective misorientation $\delta\theta$ according to equation 4.5,

$$\delta R = m\delta\theta \tag{4.5}$$

where $m = \frac{\delta R}{\delta\theta}$ is the slope at the working point on the steepest linear flank of the double crystal rocking curve (see figure 4.15).

Quantitative analysis of double crystal topographs using equation 4.5 in the approximation of the local application of the diffraction theory for perfect crystals is only applicable for crystals which are approximatively perfect over dimensions of the "effective area"(see figure 2.19) of the crystal [56].

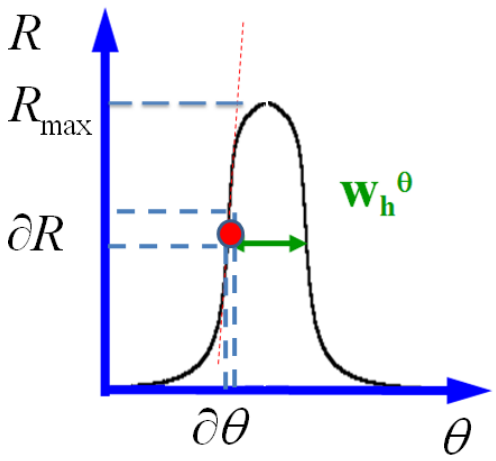

Figure 4.15: A schematic illustration of the slope of the working point on the steepest linear flank of the rocking curve. The working point has been indicated as a small dot on the left flank .

Therefore, assuming that each crystal quality was good enough ($\delta\theta << w_h^\theta$) to cause very small local variations of the reflectivity δR, the relative change in the double crystal reflectivity $\frac{\delta R}{R_{max}}$ is related to the relative change of the measured reflected x-ray intensity $\frac{\delta I^x}{I^x_{max}}$ according to equation 4.6 below.

$$\frac{\delta R}{R_{max}} = \frac{\delta I^x}{I_{max}} = \frac{m\delta\theta}{R_{max}} \tag{4.6}$$

Therefore, normalising the double crystal rocking curve (i.e. $R_{max} = 1$), equation 4.5, may be expressed as

$$\delta R = m\delta\theta = \frac{\delta I^x}{I^x_{max}} \tag{4.7}$$

Extraction of the Bragg reflected intensity from digitised topographic film images

The higher the intensity of x-rays incident on a film, the darker it became. In this way, the optical density (darkening) of the film S was assumed to be proportional to the incident Bragg reflected x-ray intensity I^x according to equation 4.8 below.

$$S = kI^x \tag{4.8}$$

The films were digitised using transmitted light through the film, and the transmitted light intensity I^L was collected on a CCD camera (see figure 4.16). The darkening of the film S absorbs light according to the Beer-Lambert law (equation 4.9). Therefore, during the film digitisation process, the transmitted light intensity through the film can be expressed as

$$S = \log_{10} \frac{I_0^L}{I^L} \tag{4.9}$$

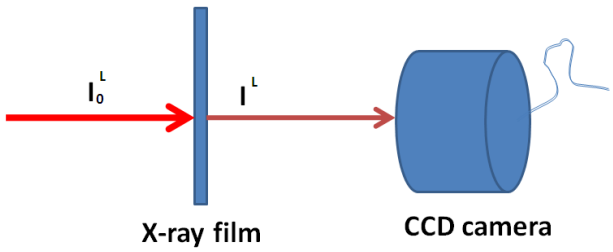

Figure 4.16: The digitisation process of the topographs. An incident light I_0^L is shone on a film and the transmitted light I^L through the film is collected on a CCD camera. The darker the film, the greater the absorption of light by the film and hence less light will be collected by camera.

Combining equation 4.8 and 4.9, the incident Bragg reflected x-ray intensity I^x is therefore proportional to the negative logarithm of the transmitted light intensity I^L.

$$\log_{10} \frac{I_o^L}{I_L} = kI^x \tag{4.10}$$

Therefore, the darker the film (due to more reflected x-ray intensity I^x absorbed by the film), the less light was collected on the CCD camera during the digitisation process. We may therefore express I^x as follows

$$I^x = \frac{1}{k} \log_{10} \frac{I_o^L}{I^L} \tag{4.11}$$

Considering the average intensity of x-rays I_{av}^x reflected by a relatively good portion of the crystal with no strain field, the relative change of the measured reflected x-ray intensity $\frac{\delta I^x}{I_{max}^x}$ may be expressed as follows

$$\frac{\delta I^x}{I_{max}^x} = \frac{I^x - I_{av}^x}{I_{max}^x} = \frac{\frac{1}{k} \log_{10} \frac{I_o^L}{I^L} - \frac{1}{k} \log_{10} \frac{I_o^L}{I_{av}^L}}{\frac{1}{k} \log_{10} \frac{I_o^L}{I_{max}^L}} = \frac{\log_{10} \frac{I_{av}^L}{I^L}}{\log_{10} \frac{I_o^L}{I_{max}^L}} \tag{4.12}$$

Where $\log_{10} \frac{I_o^L}{I_{max}^L} \equiv \log[\frac{\text{min absorption}}{\text{max absorption}}] = \log_{10}[D_R]$, and D_R is the dynamic range. Hence,

$$\frac{\delta I^x}{I_{max}^x} = \frac{1}{m} . \frac{\log \frac{I_{av}^L}{I^L}}{\log[D_R]} = \delta\theta \tag{4.13}$$

where $\delta\theta$ is the effective misorientation defined previously in equation 4.4. Equation 4.13 was used to translate the film contrast back to effective misorientation ($\delta\theta$) in the crystal lattice. Using the nitrogen concentration of

10ppb and Lang's dilatation formula (equation 2.2), the relative change of the lattice parameter $\delta d/d$ was obtained in the order of 10^8. Assuming that $\delta\theta(\vec{r})$ in equation 2.16 is only due to the local dilation, it may therefore be expressed by equation 4.14 below:

$$\delta\theta(\vec{r}) \approx -\tan\theta_B \frac{\delta d}{d}(\vec{r}) \tag{4.14}$$

Since a local adaptation of the dynamical theory for perfect crystals to distorted ones has been applied, it is important to note that this strong approximation can only be locally applied to deformed crystals when the displacement $u(r)$ is *slowly* varying such that the effective misorientation $\delta\theta(r)$ is approximately constant within the diffracting volume of the crystal [56]. In most cases, the diffracting volume is much smaller for Bragg cases and can be estimated by the penetration depth which ranges within good approximation from the extinction depth to absorption depth. For a working point on the flank of the rocking curve, it is already considerable–hundreds of micrometers. In this way, the backside of the crystal or a dislocation in all the crystal could be visualised. This only works on the wave optical level of the Takagi theory for deformed crystals [57].

Under the assumption that the dominant source of strain is an inhomogeneous impurity distribution, the maximum spatial variation of the lattice parameter is in the $\Delta d/d \sim 10^{-8}$ range. A software programme based on the dynamical theory of x-ray diffraction has specially been developed to quantify the effective misorientation. A portion of this quantification code is presented in the appendices.

Determination of the theoretical maximum slopes of the linear flanks of the double crystal rocking curves

The previous section (equation 4.5 and 4.13) required that a theoretical slope of each double crystal pair must be established. These were obtained by simulating the individual reflectivity curves for each (sample and mononochromator) crystal using the XOP software. The two separate reflectivity curves were then correlated and normalized. A derivative of the correlation function of the two curves yielded theoretical slopes for each setup. Figure 4.17 shows the double crystal rocking curves for each experimental setup. The slopes of each reflectivity curve in figure 4.17 is plotted in figure 4.18 where the maximum slope is at the steepest flank of the double crystal rocking curve. The maximum slope for each reflectivity curve is presented in table 4.2.

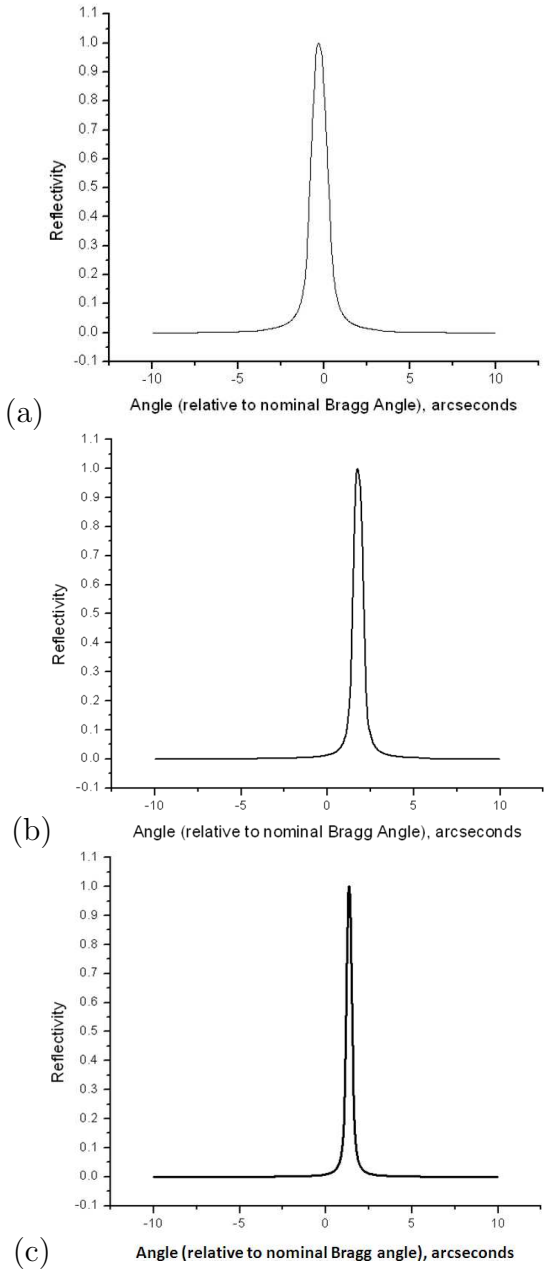

Figure 4.17: The normalised double crystal rocking curves for (a) silicon [444] and diamond [$\bar{1}$15] at 12 keV, (b) silicon [444] and diamond [$\bar{1}$15] at 16 keV, and (c) silicon [800] and diamond [800] at 20 keV respectively. These reflectivity curves were simulated using the XOP software.

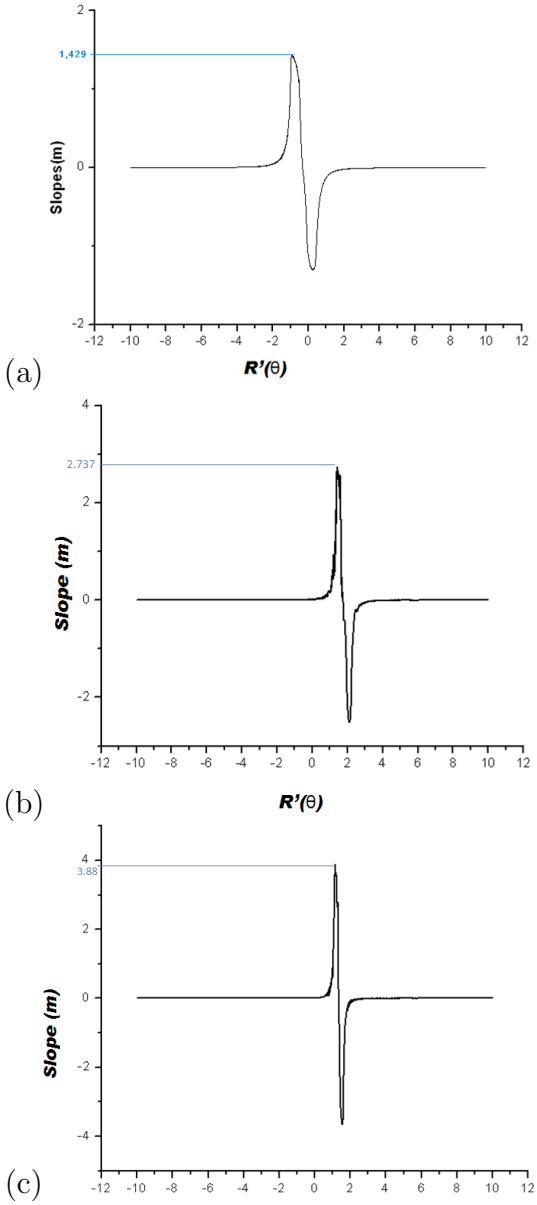

Figure 4.18: The slopes (derivatives) of the rocking curves in figure 4.17 above, namely; (a) silicon [444] and diamond [-115] at 12 keV, (b) Si [444] and diamond [$\bar{1}$15] at 16 keV and (c) silicon [800] and diamond [800] at 20 keV respectively.

Diamond $[h,k,l]$	Silicon $[h,k,l]$	Energy (keV)	Slope (rad)
$[\bar{1}15]$	[444]	12	1,429
[800]	[444]	16	2,737
[800]	[800]	20	3,880

Table 4.2: Maximum slopes of the double crystal rocking curves in figure 4.17 above.

Experimental double crystal rocking curves

Figures 4.19 – 4.22 below show experimental double crystal (figure 3.2 setup) rocking curves of the three samples under different setups (i.e different energies and reflections). The selected working point of each rocking curve has been indicated together with the topographs that will be analyzed in each case.

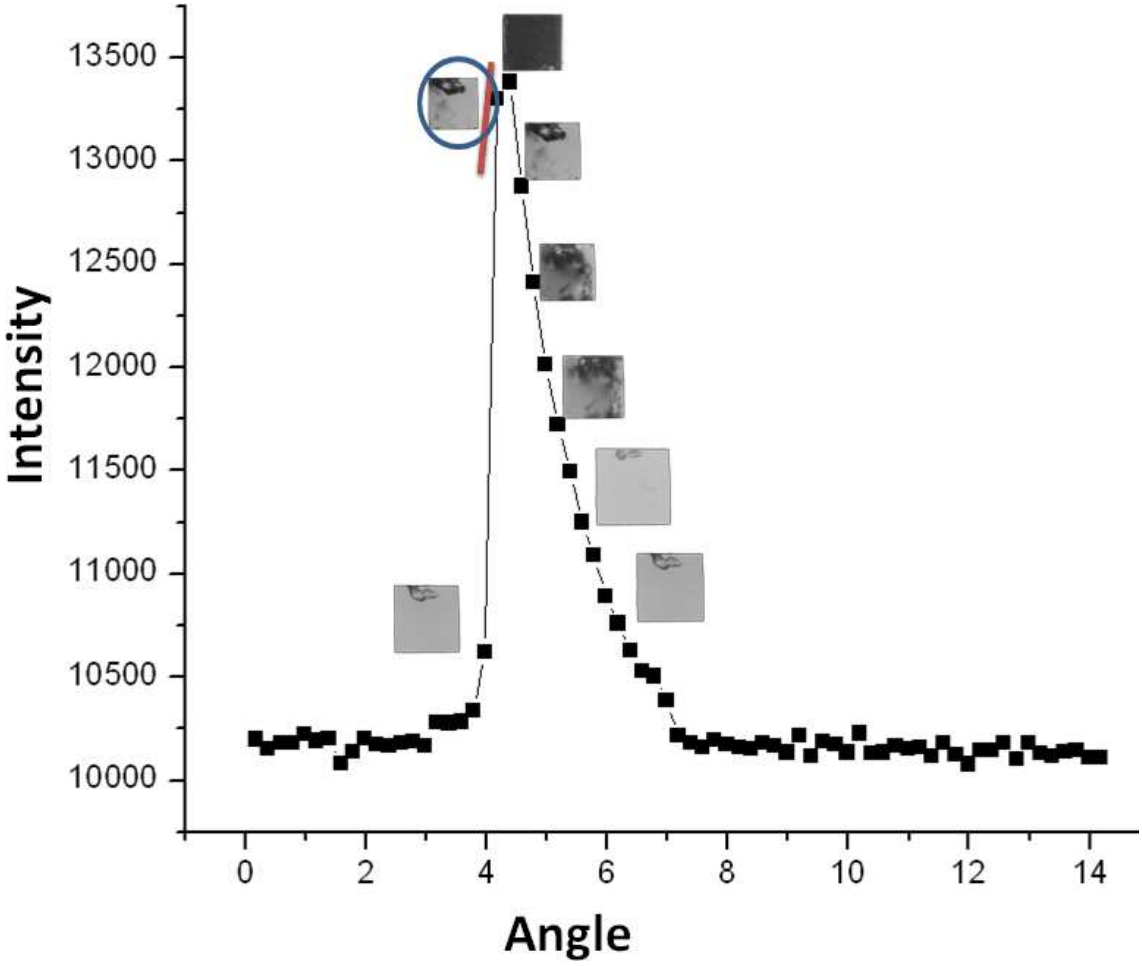

Figure 4.19: Sample 1 – A double crystal rocking curve of the silicon [800] and diamond [800] reflections at 20 keV. Higher order reflections and energy has been used to improve the strain sensitivity.

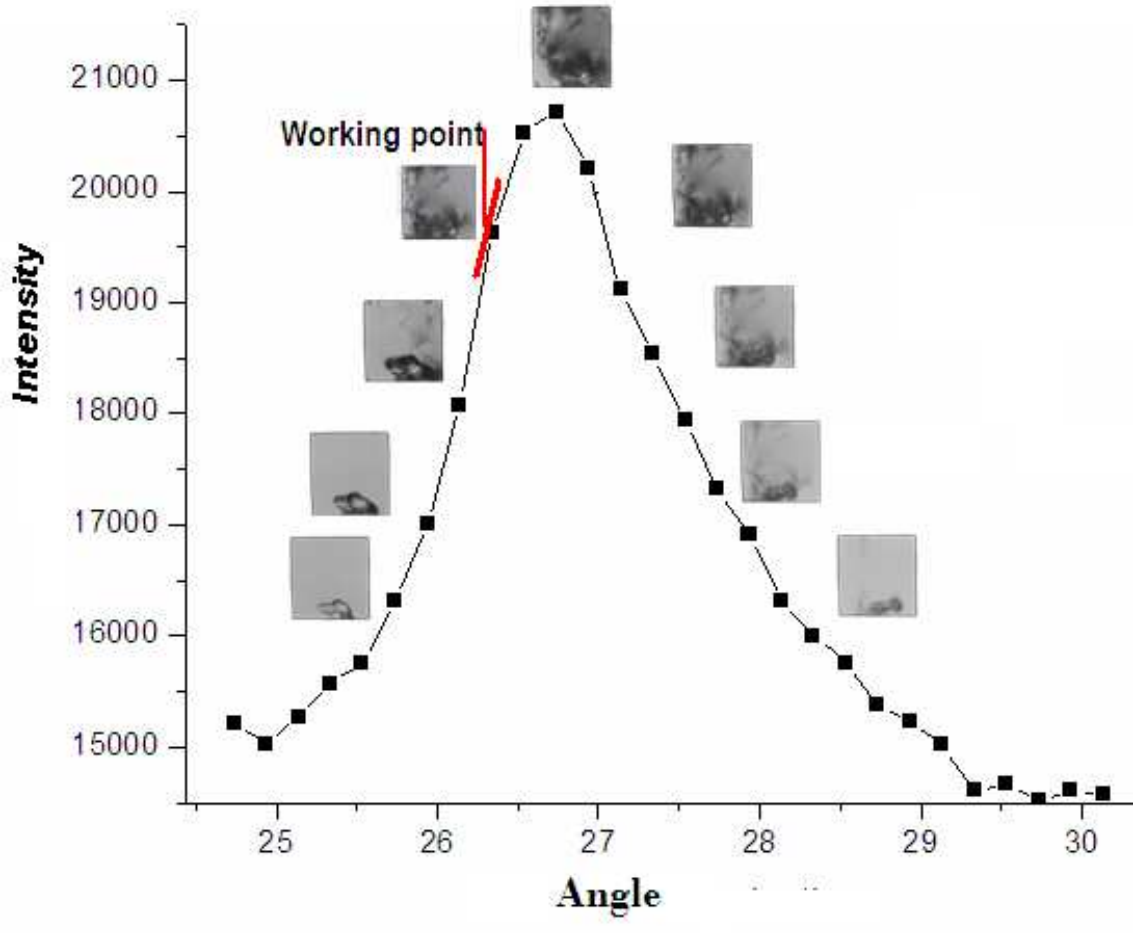

Figure 4.20: Sample 2 – A double crystal rocking curve of the silicon [800] and diamond [800] reflections at 20 keV. Higher order reflections and energy has been used to improve the strain sensitivity.

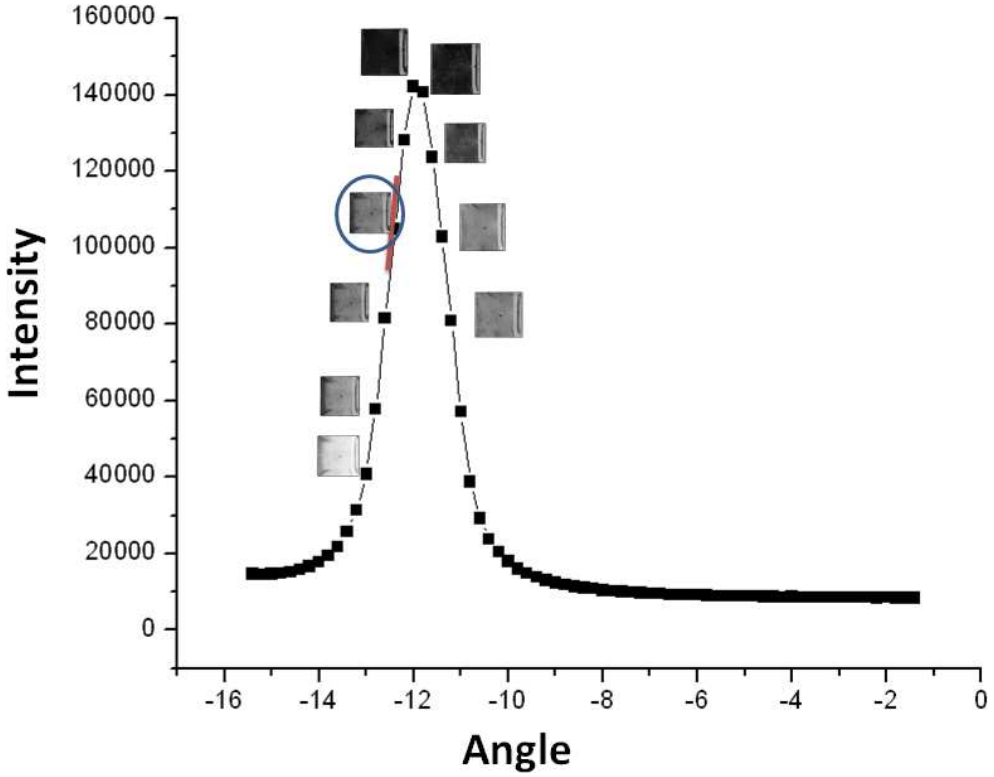

Figure 4.21: Sample 3 – A double crystal rocking curve of the [444] reflection of the silicon monochromator crystal and the [$\bar{1}$15] reflection of the diamond sample at 12 keV.

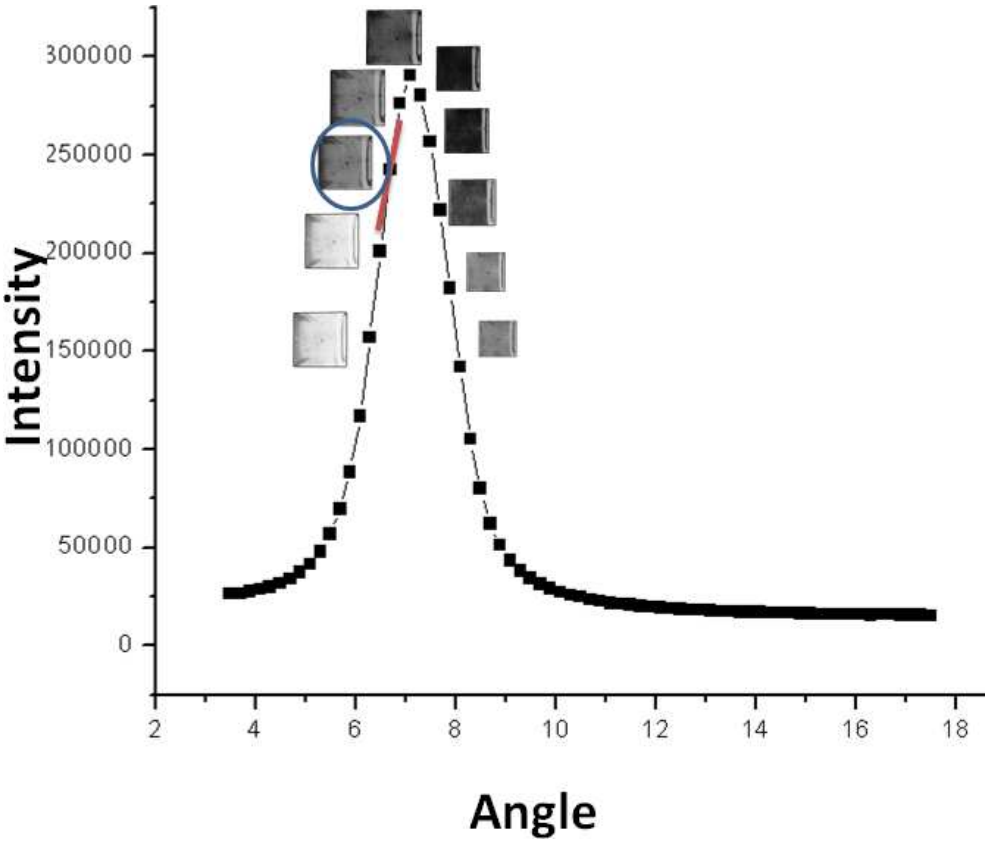

Figure 4.22: Sample 3 – A double crystal rocking curve of the [444] reflection of the silicon monochromator crystal and the [$\bar{1}$15] reflection of the diamond sample at 16 keV. The energy has been increased from 12 keV in figure 4.21 to 16 keV to improve the sensitivity.

Plane and monochromatic beam topographs selected at the working point

Sample number	*PWT Topograph*	*Diamond Reflection*	*Silicon Reflection*	*Energy keV*
1	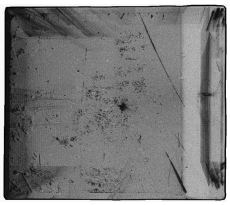	[800]	[800]	20 keV
2		[800]	[800]	20 keV
3	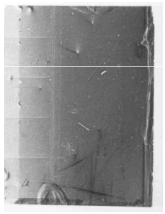	[$\bar{1}$15]	[444]	12 keV
3	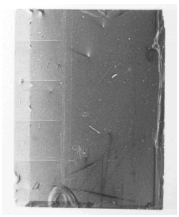	[$\bar{1}$15]	[444]	16 keV
3		[800]	[800]	20 keV

Table 4.3: Plane and monochromatic wave topographs taken at the working point on the steepest linear flanks of the double crystal rocking curves in figure 4.19–4.22.

The conversion of digitised bitmap images to grey scale values

In order to quantify this local change in Bragg angle (the effective misorientation), the digitised films were first converted to gray scale. A command line utility called "display" was used from the graphics software suite called "Image magic" obtainable from [58], to convert the digitized bitmap image of the topograph to a text (.txt) file containing gray scale values (see example in figure 4.23). The first column is the (x;y) location of the given pixel and the next group is the gray scale, which is between 2^8 and 1 for a 1 bit image and between 2^{16} and 1 for a 2 bit image.

```
0,0:    255,255,255    grey100
1,0:    243,243,243    #FEFEFE
2,0:    243,243,243    #FEFEFE
3,0:    122,122,122    #FEFEFE
```

Figure 4.23: A portion of the gray scale values obtained by conversion from the bitmap topographs using the image magic software.

The gray scale values were then read into a 2D histogram (see figure 4.24a). The physics libraries for further image manipulation were obtained from the C++ ROOT environment [59].

Correction of the non-uniform background illumination

It has been observed that the background contrasts on the topographs were not uniform. The team then decided that this was due to a non-uniform illumination during the digitization process and that they needed to correct it. This was done by modeling the non-uniform illumination over the full area from the gray scale of the differential illumination of the boundary region

of the film (where there was no sample). The numerical routine that solved the Laplace equation with the Dirichlet boundary conditions was taken from [60]. It required array of input data, and so an additional first step was to work only with a square section of the image (see figure 4.24a).

A strip of six pixels broad was taken on the boundary edge of the image away from the topograph and averaged to form the boundary values for each of the four sides as shown in figure 4.24(b). This thin and almost invisible boundary was later used to reconstruct the non uniform background shown by figure 4.24(c) by regarding it as the Dirichlet boundary conditions of the Laplace problem in 2D. The model therefore imagined the problem was represented by a Poisson equation (with Dirichlet boundary conditions) with no internal charge where the boundary conditions are the gray scale of the illumination of the edge of the picture where there is no topograph information from the diamond. The solution of Poisson equation would then reconstruct the background illumination as if there was no diamond. The non-uniform background was then normalised out of the original image by dividing through and rescaling (figure 4.24d). The highest point in the background histogram was used as the fixed point in the normalization.

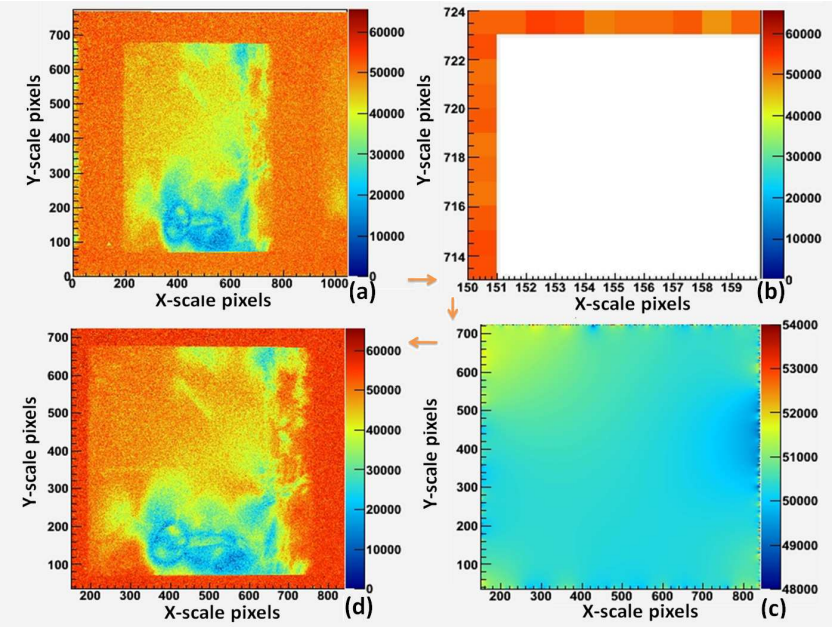

Figure 4.24: Correction of the non-uniform background illumination. (a) a 2D histogram of the image from the gray scale values, (b) a strip of six pixels broad taken on the boundary edge of the image away from the topograph and averaged to form the boundary values for each of the four sides, (c) a reconstruction of the entire non-uniform background illumination by solving the Laplace problem for the interior points using the illumination at the boundary points and (d) a square histogram with corrected background illumination.

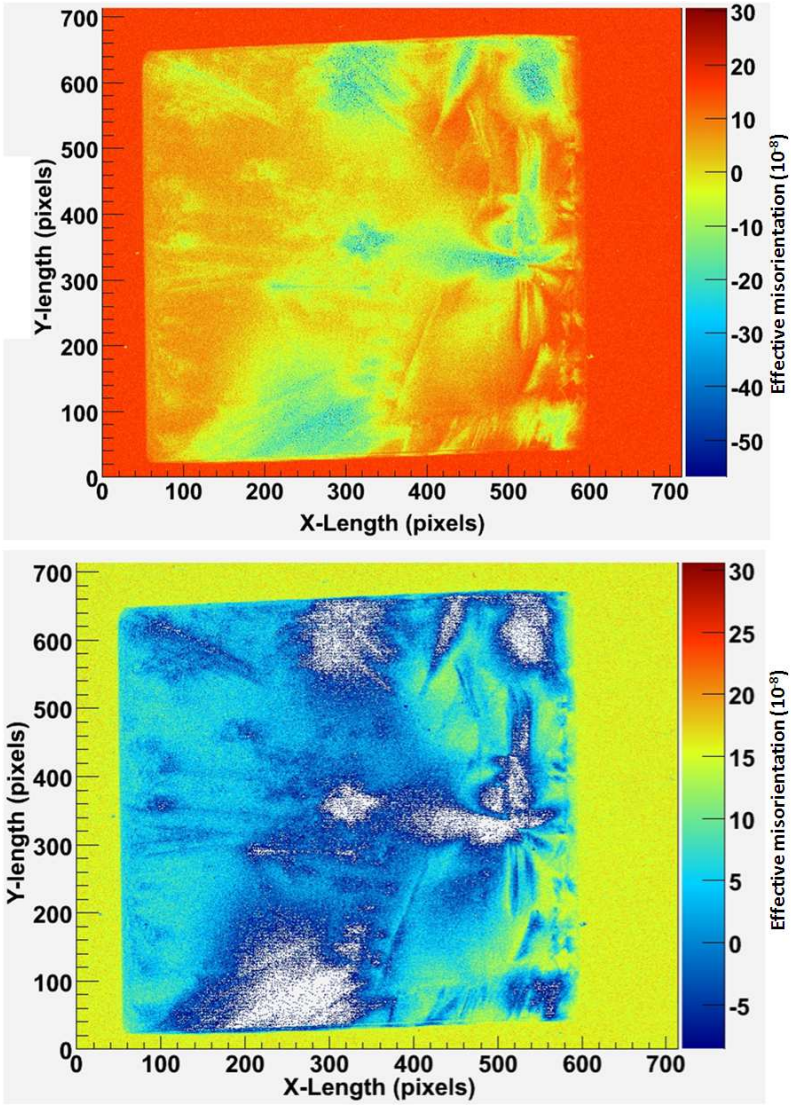

Figure 4.25: Sample 1 : A quantified topograph of the [800] diamond reflection at 20 keV. The [800] silicon monochromator crystal reflection was used in a double crystal setup. The y-scale in the bottom image was slightly altered (zoomed in) to focus more on the weaker strain fields. The strain sensitivity is in the order of 10^8.

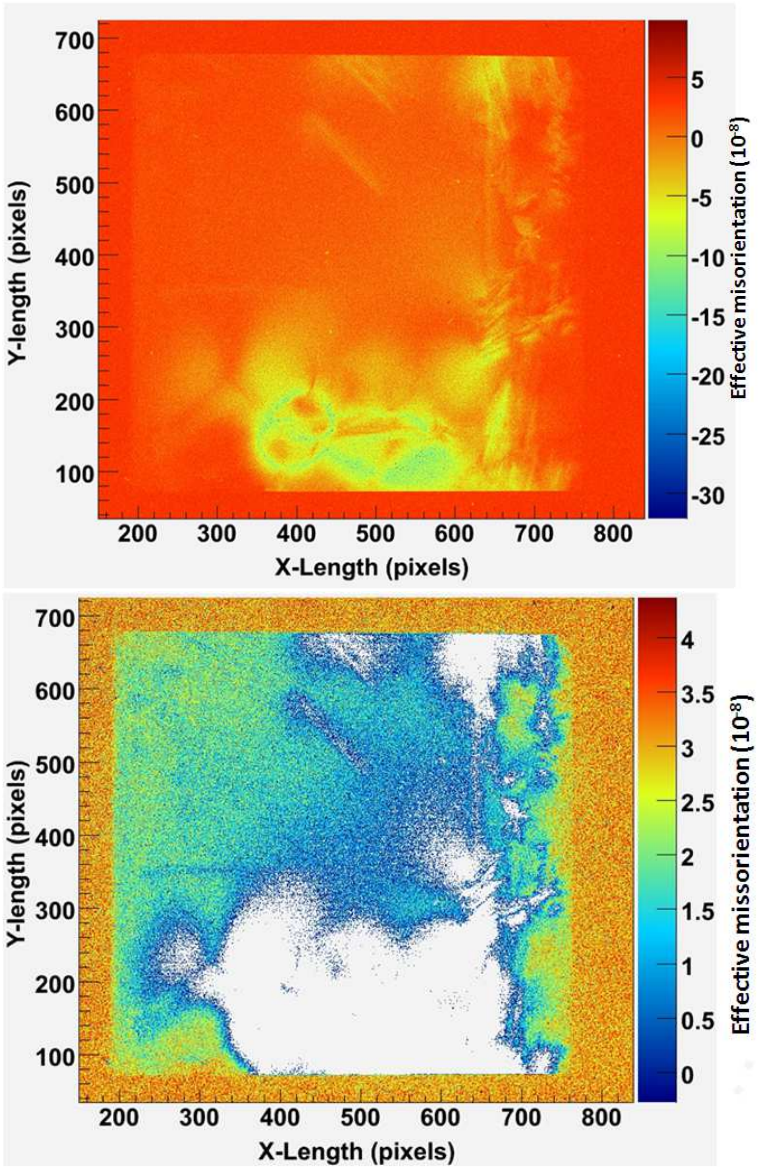

Figure 4.26: Sample 2 : A calibrated topograph of the diamond [800] reflection taken with the silicon [800] reflection at 20 keV. The y-scale of the bottom image has been slightly altered (zoomed in) to focus more on the weaker strain fields. The strain sensitivity is in the order of 10^{-8}.

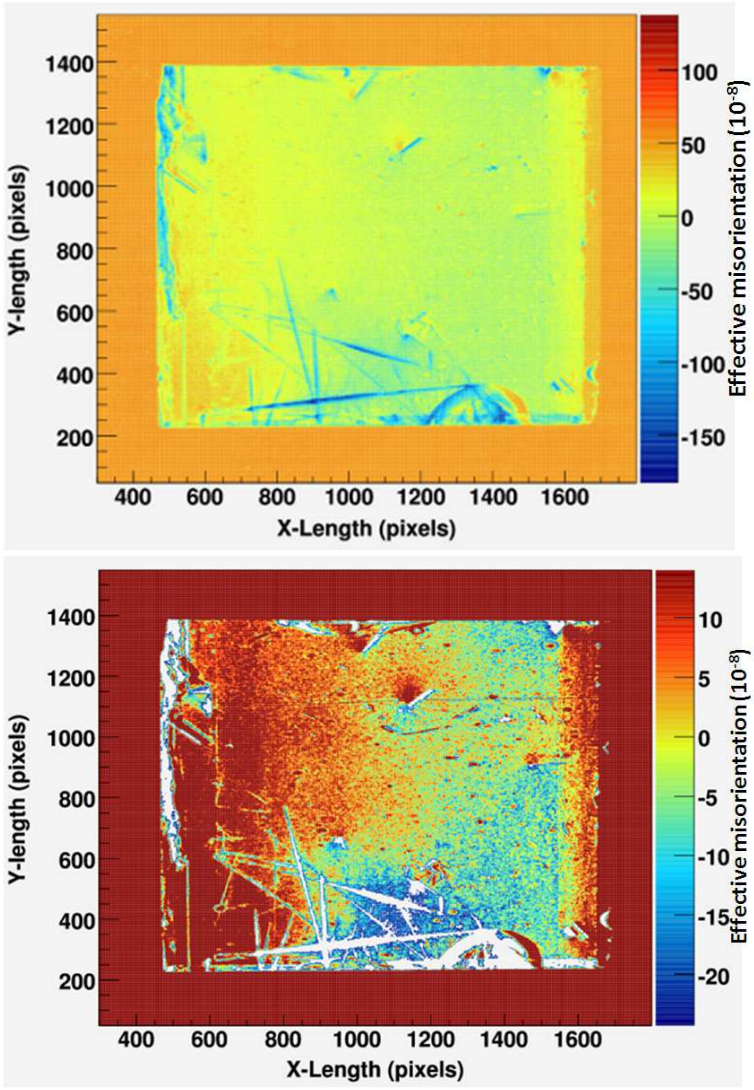

Figure 4.27: Sample 3 : A quantified topograph of a diamond [$\bar{1}$15] reflection taken with the silicon monochromator crystal 444-reflection at 12 keV. The y-scale of the bottom image has been slightly altered (zoomed in) to focus more on the weaker strain fields.

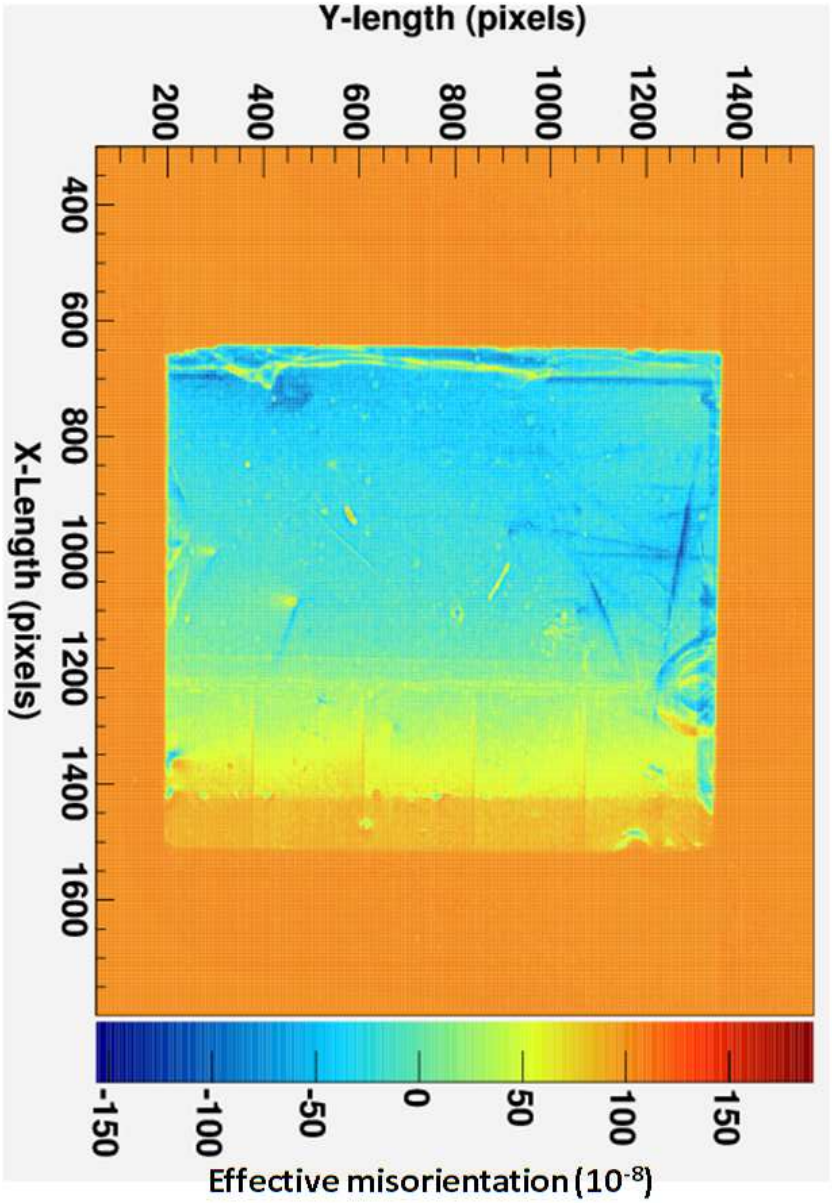

Figure 4.28: Sample 3 : A calibrated topograph of the diamond [$\bar{1}$15] reflection taken with the [444] reflection of the silicon monochromator crystal in a double crystal setup at 16 keV. The energy has been increased from 12 keV to 16 keV to slightly improve the strain sensitivity.

Sample 1

Only the [800] reflection of sample 1 (figure 4.25) which has been taken at 20keV using the [800] silicon reflection has been analyzed. On the bottom image of figure 4.25, the scale is zoomed only between -5×10^{-8} and 20×10^{-8} thereby eliminating the overly strained sections of the topograph pixels and around the top right hand corner of the topograph.

Sample 2

Figure 4.26 is the [800] reflection of the second sample also taken at 20keV using the [800] monochromator crystal reflection. The sample is heavily strained on the bottom right corner and just along the right edge. This sample has relatively fewer strains on the top left hand corner. The bottom image of figure 4.26 focuses on this low strain region. The maximum effective misorientation in this region is around $6,5\times10^{-8}$.

Sample 3

The $[\bar{1}15]$ and [800] reflections of sample three have been analyzed. The $[\bar{1}15]$ reflection (Figure 4.27) was taken at 12keV using the Si[444] reflection and at 16keV (figure 4.28) using the Si[444] reflection.

Chapter 5

Conclusion

HPHT synthetic diamonds have been studied using x-ray topography. Type Ib material with a nitrogen content of a few hundred parts per million and required size of 4 to 8 mm^2 is of too low quality. Type Ib materials have for many years been assumed to be the best candidate for applications in synchrotrons because of their larger size, and because it was hoped that uniform N incorporation could lead to sufficient lattice quality. Only selected samples of that type may be used for less demanding applications like phase plates[61].

Advances in HPHT synthesis methods have allowed the growth of type IIa diamond crystals of almost the same size as the type Ib, but with substantially lower nitrogen content. From the initial characterisation of this new product, high purity (very low nitrogen content) type IIa diamond crystals, the researchers are able to report that the crystalline (bulk) perfection of some of the HPHT grown materials is approaching the quality required for the more demanding applications such as imaging applications with coherence preservation. However, for a coherence preserving crystal, both the bulk and the surface quality must be sufficiently high. The material studied so

far in this work was of high bulk quality and the currently best surface finish obtained by mechanical polishing was measured on a type Ib sample with a value of 0.3 nm rms.

The type IIa HPHT diamond quality proved to be too high to be quantified by rocking curve mapping. Rocking curve measurements carried out with a high resolution setup showed negligible or only small increases ($0.0''$ to $0.2''$) of local rocking curve widths ($1''$) after extraction of the apparatus function (width about $0.15''$), see table 4.1. The rocking curve maps display essentially the Darwin line width in the central cubic growth sector, which appears essentially free of extended defects.

The samples exhibit very good bulk properties in the central cubic growth sector which improve with distance from the seed face. The relationship of extended defects to growth sectoring has been noted. The more sensitive monochromatic beam topography does not see contrast across growth sector boundaries of the low strain HPHT type IIa diamonds. This means that the lattice dilatation due to the nitrogen concentration change across the boundary is less than the minimum detection limit of the monochromatic beam topography for effective misorientation. No strain fields related to growth sector boundaries are visible in the central region when using the white beam technique. The central region of each topograph generally shows no extended defects

Instead, monochromatic beam topography quantitative mapping of the strain was developed to a high degree of strain sensitivity. Successive high-order reflections and correspondingly higher energy x-rays were used to increase

the steepness of the rocking curve at the working point, thereby increasing the strain sensitivity of the plane and monochromatic wave topography technique. The strain fields of certain defects had a clearly visible macroscopic extent. The maximum spatial variation of the lattice parameter is in the $\Delta d/d \sim 10^{-8}$ range.

Bibliography

[1] R.C. Burns, V. Cvetkovic, C.N. Dodge, D.J.F. Evans, T. Rooney Marie-Line, P.M. Spear, and C.M. Welbourn. Growth-sector dependence of optical features in large synthetic diamonds. *Journal of Crystal Growth*, 104(2):257 – 279, 1990.

[2] J.P. Blewett. Synchrotron radiation – early history. *Journal of Synchrotron Radiation*, 5(3):135–139, May 1998.

[3] F.R. Elder, R.V. Langmuir, and H.C. Pollock. Radiation from electrons accelerated in a synchrotron. *Phys. Rev.*, 74(1):52–56, Jul 1948.

[4] F. Masiello. Characterization of high pressure high temperature diamond single crystals using synchrotron radiation. Master's thesis, Universit'A Degli Studi di Torino, 2007.

[5] http://www xfel.spring8.or.jp. SPring-8 compact SASE source. *SASE-FEL*, Sep 2008.

[6] D.E. Moncton. Towards a fourth-generation light source. In *Proceedings of the 1999 Solid State Sciences Committee Forum*, volume 1999, pages 38 – 40. National Academic Press, 1999.

[7] Y. Ando and N. Kato. X-ray diffraction phenomena in elastically distorted crystals. *Journal of Applied Crystallography*, 3(2):74–89, Mar 1970.

[8] R.C. Burns, A.I Chumakov, S.H. Connell, D. Dube, H.P. Godfried, J.O. Hansen, J. Härtwig, J. Hoszowska, F. Masiello, L. Mkhonza, M. Rebak, A. Rommevaux, R. Setshedi, and P. Van Vaerenbergh. HPHT growth and x-ray characterization of high-quality type IIa diamond. *Journal of Physics: Condensed Matter*, 21(36):364224, 2009.

[9] R.C. De Vries. The science behind the synthesis of diamond. *J.Mater.Educ.*, 13:387–440, 1991.

[10] M. Hart and L. Berman. X-ray optics for synchrotron radiation perfect crystals, mirrors and multilayers. *Acta Crystallographica Section A*, 54(6 Part 1):850–858, Nov 1998.

[11] O. Hignette, P. Cloetens, G. Rostaing, P. Bernard, and C. Morawe. Efficient sub 100 nm focusing of hard x rays. *Review of Scientific Instruments*, 76(6):063709, 2005.

[12] A.J. SINGH. Beryllium-the extraordinary metal. *Mineral Processing and Extractive Metallurgy Review*, 13(1):177–192, 1994.

[13] A.K. Freund. Diamond single crystals: the ultimate monochromator material for high-power x-ray beams. *Optical Engineering*, 34(2):432–440, 1995.

[14] A.I. Chumakov, R. Rüffer, O. Leupold, A. Barla, H. Thiess, T. Asthalter, B.P. Doyle, A. Snigirev, and A.Q.R. Baron. High-energy-resolution x-ray optics with refractive collimators. *Appl. Phys. Lett.*, 77(1):31 – 33, 2000.

[15] J. Hoszowska, A.K. Freund, E. Boller, J.P.F. Sellschop, G. Leve, J. Härtwig, R.C. Burns, and M. Rebak. Characterisation of synthetic diamond crystals by spatially resolved rocking curve measurements. *Phys. J*, 34:A47–A51, 2001.

[16] Y. Zhao, Z. Li, X. Tiqiao, and X. Shaojian. Principle of π-phase plate long trace profiler for synchrotron radiation optics. *Optics Communications*, 200:23–26, Dec 2001.

[17] J.E. Field. *Properties Of Diamond*. Academic Press, 1979.

[18] J.P.F. Sellschop, S.H. Connell, A.K. Freund, J. Hoszoska, C. Detlefs, R.C. Burns, M Rebak, J.O. Hansen, and C.E. All. Synchrotron x-ray applications of synthetic diamonds. *New Carbon Frontier Carbon Technology*, 5:253–280, 2000.

[19] H.T. Hall. The synthesis of diamond. *J. Chemical Education*, 38:1 – 7, 1961.

[20] S.T. Lee, Z. Lin, and X. Jiang. CVD diamond films: nucleation and growth. *Materials Science and Engineering*, 25:123 – 154, 1999.

[21] E.G. Lundblad. High pressure synthesis of diamond in Sweden in 1953. In S. C. Schmidt, J. W. Shaner, G. A. Samara, and M. Ross, editors, *High-pressure science and technology—1993*, volume 309, pages 503–506. AIP, 1994.

[22] F.P. Bundy, H.T. Hall, H.M. Strong, and R.H. Wentorf. Man-made diamonds. *Nature*, 176:51–55, 1955.

[23] D. Altin, J. Härtwig, R. Köhler, W. Ludwig, M. Ohler, and H. Klein. X-ray diffraction topography using a diffractometer with a bendable

monochromator at a synchrotron radiation source. *J. Synchrotron Rad.*, 9(5):282 – 286, 2002.

[24] H. Kanda. Growth of high pressure synthetic diamonds. *Journal of The Gemmological Society of Japan*, 20:37 – 46, 1999.

[25] V. Dolmatov. On the mechanism of detonation nanodiamond synthesis. *Journal of Superhard Materials*, 30:233–240, 2008. 10.3103/S1063457608040023.

[26] H.O. Pierson. *Handbook of Carbon, Graphite, Diamond and Fullerenes - Properties, Processing and Applications*. William Andrew Publishing/Noyes, Apr 13 1993.

[27] R. C. Burns and G. J. Davies. *The Properties of Natural and Synthetic Diamond*. Academic New York, 1992.

[28] R.C. Burns, J.O. Hansen, R.A. Spits, M. Sibanda, C.M. Welbourn, and D.L. Welch. Growth of high purity large synthetic diamond crystals. *Diamond Related Material*, 8:1433 – 1437 – 5, 1999.

[29] F.P. Bundy. The pressure-temperature phase and transformation diagram for carbon updated through 1994. *Carbon*, 34(2):141 – 153, 1996.

[30] H. Kanda. Nonuniform Distribution of colour and luminiscence of diamond single crystals. *New Diamond and Frontier Carbon Technology*, 17:105–106, 2007.

[31] L. Berman, J.B. Hastings, D.P. Siddons, M. Koike, V. Stojanoff, and M. Hart. Diamond crystal x-ray optics for high-power-density synchrotron radiation beams. *Nucl. Instr. & Meth. A*, 329:555 – 563, 1993.

[32] T.C. Alan. Things we still don't know about optical centers in diamond. *Diamond and Related Materials*, 8:1455–1462, January 1999.

[33] K. Watanabe, S.C. Lawson, H. Isoya, J. Kanda, and Y. Sato. Phosphorescence in high-pressure synthetic diamond. *Diamond and Relaled Materials*, 1(5):99–106, Nov 1997.

[34] J.P.F. Sellschop, Freund.A., J. Hosxowka, S.H. Connell, M. Rebak, and R.C. Burns. The quest for diamond crystal perfection to meet the needs of physics: Unrealistic dream or attainable target. *Phys. Stat. Solidi A*, 3:415–422, 2002.

[35] M. Moore. Synchrotron x-ray topography. *Radiation Physics and Chemistry*, 45:427–444, mar 1995.

[36] J. Härtwig, V. Holý, R. Kittner, J. Kubêna, and V. Lerche. Investigation of quartz crystals with non-homogeneous distributions of impurity atoms by x-ray methods. *Phys. Stat. Solidi A*, 105:61 – 75, 1988.

[37] D.K. Bowen and B.K. Tanner. *High Resolution X-Ray Diffractometry and Topography.* Taylor & Francis, 1998.

[38] C. Suryanarayana and M. Grant Norton. *X-Ray diffraction: a practical approach.* Plenum Press, 1998.

[39] J. Daillant and A. Gibaud. *X-Ray and Neutron Reflectivity: Principles and Applications.* Springer, 1999.

[40] C. Darwin. Theory of x-ray reflection. *Philos.Mag.*, 27:315–333, 1914.

[41] C. Darwin. Theory of x-ray reflection, Part II. *Philos.Mag.*, 27:675–690, 1914.

[42] M.V. Laue. Die dynamische Theorie der röntgenstrahlinter-ferenzen in neuer Form. *Ergeb.Exact.Naturwiss*, 10:133–158, 1931.

[43] W. Bartels, J. Hornstra, and D. Lobeek. X-ray diffraction of multilayers and superlattices. *Acta Crystallographica Section A*, 42(6):539–545, Nov 1986.

[44] http://www.esrf.fr/UsersAndScience/Experiments/ Imaging/ID19. X-ray diffraction imaging (x-ray topography). An overview about techniques and applications. *ESRF*, January 2007.

[45] http://www.tf.uni kiel.de. Perspective view of a dislocation. *University of Kiel*, June 2010.

[46] R. Berman. *Physical properties of diamond*. Clarendon Press, 1965.

[47] W. Berg. 1931 examination of the lattice disturbances in crystals naturwissenschaften 19 3916 (in german). *Naturwissenschaften(in German)*, 19:391–396, 1931.

[48] C. Barrett. A new microscopy and its potentialities trans. *AIME*, 161:1564, 1945.

[49] A.R. Lang. Direct observation of individual dislocations by x-ray diffraction. *Journal of Applied Physics*, 29(3):597–598, 1958.

[50] P.M. Martineau, M. P. Gaukroger, K. B. Guy, S.C. Lawson, D. J. Twitchen, I. Friel, J.O. Hansen, G.C. Summerton, T.P.G. Addison, and R. Burns. High crystalline quality single crystal chemical vapour deposition diamond. *Journal of Physics: Condensed Matter*, 21:36, 2009.

[51] W. Wierzchowski and M. Moore. Bragg-case images of stacking faults. *Acta Crystallography*, A 51:83140, 1995.

[52] http://rsbweb.nih.gov/ij/download.html. Image magic download. *NIH Image*, June 2008.

[53] A.T. Macrander, S. Krasnicki, Y. Zhong, J. Maj, and Y.S. Chu. Strain mapping with parts-per-million resolution in synthetic type-ib diamond plates. *Applied Physics Letters*, 87(19):194113, 2005.

[54] M. Moore. Synchrotron x-ray topography. *Radiation Physics and Chemistry*, 45:427–443, 1995.

[55] R.C. Burns, A.I. Chumakov, S.H. Connell, D. Dube, H.P. Godfried, J.O. Hansen, J. Härtwig, J. Hoszowska, F. Masiello, L. Mkhonza, M. Rebak, A. Rommevaux, R. Setshedi, and P. Van Vaerenbergh. HPHT - grown type IIa diamond as a material for synchrotron beam line optical elements. *Ref. No.: 07-2223-DRM*, 1, 2008.

[56] J. Kuběna and V. Holý. Investigation of the growth striations in silicon by x-ray topography. *Czechoslovak Journal of Physics*, 33:1315–1322, 1983. 10.1007/BF01590221.

[57] J. Härtwig. Hierarchy of dynamical theories of x-ray diffraction for deformed and perfect crystals. *Journal of Physics D: Applied Physics*, 34(10A):A70–A77, 2001.

[58] http://mirror.is.co.za/pub/imagemagick/www/binary-releases.html. Introduction to imagemagick. *Image Magic*, June 2010.

[59] http://root.cern.ch. Downloading root. *CERN*, May 2007.

[60] http://www.nr.com/. The art of scientific computing, third edition (2007). *Cambrige University*, May 2006.

[61] http://www.esrf.eu/UsersAndScience/Publications/Highlights/2005 /Imaging/XIO5. X-ray diffraction imaging (x-ray topography). An overview about techniques and applications diamonds for Modern Synchrotron Radiation sources. *ESRF*, January 2010.

Appendices

Appendix A

Analysis software

```
//-------------------------Quantify (see pg 28 and 210 of Bowen and Tanner)-----------------
        Float_t H_average;                      // Average value of the bitmap
        slope = slope * (3600 * 180 / 3.14159); //convert  from 1/arcseconds to 1/radians
        Int_t n_points = 0;
        temp = 0;
        for (i=nbins/4;i<=3*nbins/4;i++)
        {
                for (j=nbins/4;j<=3*nbins/4;j++) {
                        temp=temp+hcor2->GetBinContent(i,j);
                        n_points = n_points + 1;
                }
        }
        H_average = temp / n_points;
        cout << "the average central section of the topograph intensity is "<<H_average<<"\n";


        TH2F *hcal2 = new TH2F("hcal2","Calibrated Histogram (10^-8)",nbins,Axis_t(xlow+nbinsx_0)
        //,Axis_t(xlow+nbinsx_0+nbins-1),
                                nbins,Axis_t(ylow+nbinsy_0),Axis_t(ylow+nbinsy_0+nbins-1));
        for (i=1;i<=nbins;i++)
        {
                for (j=1;j<=nbins;j++) {
                        temp = log(hcor2->GetBinContent(i,j)/H_average)/log(dyn_range)/slope*1.0e8;
                        hcal2->SetBinContent(i,j,temp);
                }
        }


cout << "\n\n Drawing image with Quantification \n";

        MyCanvas->WaitPrimitive();   /* Waits untill you click the middle
                                        mouse button in the graphics window */

        MyCanvas->Divide(1,1);
        MyCanvas->Clear();
        MyCanvas->cd(1);  //drawing original data on the 1st canvas
        gPad->SetRightMargin(0.2);
        gPad->SetLeftMargin(0.15);

        gPad->SetBottomMargin(0.12);
        hcal2->SetContour(255);
        set_plot_style();
        hcal2->SetStats(kFALSE);
        hcal2->GetXaxis()->SetTitle("X-Length (pixels)");
        hcal2->GetYaxis()->SetTitle("Y-length (pixels) ");
        hcal2->GetZaxis()->SetTitle("Eff misorientation (10^{-8})");
        hcal2->GetXaxis()->CenterTitle();
        hcal2->GetYaxis()->CenterTitle();
        hcal2->GetZaxis()->CenterTitle();
        hcal2->GetXaxis()->SetTitleOffset(1.2);
        hcal2->GetYaxis()->SetTitleOffset(1.5);
        hcal2->GetZaxis()->SetTitleOffset(1.5);
        hcal2->DrawCopy("colz");

        MyCanvas->Update();

        MyCanvas->WaitPrimitive();   /* Waits untill you click the middle
                                        mouse button in the graphics window */
```

Figure A.1: A portion of the C++ code used for the quantification of the plane and monochromatic plane topographs.

Appendix B

Scholarly research outputs

International Conferences- 2005

1. S.H. Connell, R. K. Setshedi, D. Dube, L. Mkhonza, M. Rebak,. J. Härtwig, J. Hoszowska, R.C. Burns, J.O. Hansen, *High Crystal Quality Diamond studied by a variety of synchrotron generated X-ray techniques*ADC/Nano Carbon 8th International Conference on Applications of Diamond and Related Materials –1st NanoCarbon Joint Conference Argonne National Laboratory May 15–19, 2005.

2. R.K. Setshedi, D. Dube, L. Mkhonza, M. Rebak, S. H. Connell, R. Burns, J. Hansen, J. Härtwig and J. Hoszowska, *High Crystal Quality Diamond studied with a variety of synchrotron generated X-ray techniques.* St. Catherine's College Oxford. Diamond Conference 2005, 13-15 July 2005,

3. J. Härtwig, J. Hoszowska, P. Van Vaerenbergh, I. Gierz, S.H. Connell, M. Rebak, R. Setshedi, D. Dube, L. Mkhonza, R. Burns, J.O. Hansen, *Diamond and the future X-ray optics developments*Optics & Photonics, San Diego, California USA, 31st July 4th August 2005,

4. J.O. Hansen, R. Burns, H. Godfried, M. Rebak, S.H. Connell, J. Härtwig, P. Van Vaerenbergh, I. Gierz, J. Hoszowska, A. Freund. *Performance of*

HPHT grown type IIa diamond as a material for synchrotron beam line optical elements Diamond at work Conference Barcelona 20-21 October 2005

5. R. K. Setshedi, D. Dube, L. Mkhonza, M. Rebak, S. H. Connell, R. Burns, J. Hansen J. Härtwig, J. Hoszowska *Diamond beam optics for high brilliance X-ray beams from* 3rd *and* 4th *generation synchrotrons.* US-Africa Advanced Studies Institute on Photon Interactions with Atoms and Molecules, November 3–12, 2005 in Durban, South Africa.

LOCAL CONFERENCES 2005

1. L. Mkhonza, S. H. Connell, D. Dube, R. K. Setshedi, J. Härtwig and J. Hoszowska *Spatial coherence preservation by HPHT synthetic single diamond crystals using synchrotrons x-ray beam*, South African Institute of Physics, 2005

2. D. Dube, S.H. Conell, L. Mkhonza, R. Setshedi, J.O. Hansen, R.J. Caveney, J. Härtwig, J. Hoszowska, P. Van Vaerenbergh. *Synchrotron surface characterisation of ultra high quality HPHT Type IIa synthetic diamonds.*, South African Institute of Physics, 2005

3. R Setshedi, D. Dube, L. Mkhonza, S.H. Connell, J. Hansen, R. Burns, J. Härtwig, J. Howzoska, *High Resolution Synchrotron X-ray Rocking Curve Mapping and various X-ray topographies of very high quality diamond*, South African Institute of Physics, 2005

IN-HOUSE PRESENTATIONS

1. The theory of Relativity

2. The history of Synchrotron Radiation Sources

3. Free electron lasers (SASE-FEL)

4. Applications of diamond beam optic elements in 3rd and 4th generation synchrotron radiation facilities

INTERNATIONAL SCHOOLS ATTENDED

1. Synchrotron radiation and free electron lasers– Brunnen, Switzerland, 2-9 July 2003